AD/A-003 689

THEORETICAL AND EXPERIMENTAL STUDIES OF THE SHAPED-CHARGE PHENOMENON

Foreign Technology Division
Wright-Patterson Air Force Base, Ohio

20 November 1974

AD/A - 003689

DOCUMENT CONTROL DATA - R & D

(Security classification of title, body of abstract and indexing annotation must be entered when the overall report is classified)

1 ORIGINATING ACTIVITY (Corporate author)	2a. REPORT SECURITY CLASSIFICATION
Foreign Technology Division Air Force Systems Command U. S. Air Force	Unclassified
	2b. GROUP

3 REPORT TITLE

THEORETICAL AND EXPERIMENTAL STUDIES OF THE SHAPED-CHARGE PHENOMENON

4 DESCRIPTIVE NOTES (Type of report and inclusive dates)

Translation

5 AUTHOR(S) (First name, middle initial, last name)

Author Unknown

6 REPORT DATE	7a. TOTAL NO. OF PAGES	7b. NO OF REFS
1953	79	45
8a. CONTRACT OR GRANT NO.	9a. ORIGINATOR'S REPORT NUMBER(S)
b. PROJECT NO	FTD-HC-23-2850-74
c.	9b. OTHER REPORT NO(S) (Any other numbers that may be assigned this report)
d.	

10 DISTRIBUTION STATEMENT

Approved for public release;
distribution unlimited.

11 SUPPLEMENTARY NOTES	12 SPONSORING MILITARY ACTIVITY
	Foreign Technology Division Wright-Patterson AFB, Ohio

13 ABSTRACT

20

DD FORM 1473 NOV 65

EDITED TRANSLATION

FTD-HC-23-2850-74   20 November 1974

THEORETICAL AND EXPERIMENTAL STUDIES OF THE
SHAPED-CHARGE PHENOMENON

By: Author Unknown

English pages: 74

Source: Mekhanika, Vol. 20, No. 4, 1953,
         pp. 51-105

Country of Origin: USSR
Translated by: F33657-72-D-0853-0006
Requester: FTD/PDTN
Approved for public release;
distribution unlimited.

PREPARED BY:

TRANSLATION DIVISION
FOREIGN TECHNOLOGY DIVISION
WP-AFB, OHIO.

FTD-HC-23-2850-74   Date 20 Nov 1974

All figures, graphs, tables, equations, etc. merged into

this translation were extracted from the best quality

copy available.

U. S. BOARD ON GEOGRAPHIC NAMES TRANSLITERATION SYSTEM

Block	Italic	Transliteration	Block	Italic	Transliteration
А а	А а	A, a	Р р	Р р	R, r
Б б	Б б	B, b	С с	С с	S, s
В в	В в	V, v	Т т	Т т	T, t
Г г	Г г	G, g	У у	У у	U, u
Д д	Д д	D, d	Ф ф	Ф ф	F, f
Е е	Е е	Ye, ye; E, e*	Х х	Х х	Kh, kh
Ж ж	Ж ж	Zh, zh	Ц ц	Ц ц	Ts, ts
З з	З з	Z, z	Ч ч	Ч ч	Ch, ch
И и	И и	I, i	Ш ш	Ш ш	Sh, sh
Й й	Й й	Y, y	Щ щ	Щ щ	Shch, shch
К к	К к	K, k	Ъ ъ	Ъ ъ	"
Л л	Л л	L, l	Ы ы	Ы ы	Y, y
М м	М м	M, m	Ь ь	Ь ь	'
Н н	Н н	N, n	Э э	Э э	E, e
О о	О о	O, o	Ю ю	Ю ю	Yu, yu
П п	П п	P, p	Я я	Я я	Ya, ya

* ye initially, after vowels, and after ъ, ь; e elsewhere.
When written as ё in Russian, transliterate as yё or ё.
The use of diacritical marks is preferred, but such marks
may be omitted when expediency dictates.

iii

FOLLOWING ARE THE CORRESPONDING RUSSIAN AND ENGLISH

DESIGNATIONS OF THE TRIGONOMETRIC FUNCTIONS

Russian	English
sin	sin
cos	cos
tg	tan
ctg	cot
sec	sec
cosec	csc
sh	sinh
ch	cosh
th	tanh
cth	coth
sch	sech
csch	csch
arc sin	$\sin^{-1}$
arc cos	$\cos^{-1}$
arc tg	$\tan^{-1}$
arc ctg	$\cot^{-1}$
arc sec	$\sec^{-1}$
arc cosec	$\csc^{-1}$
arc sh	$\sinh^{-1}$
arc ch	$\cosh^{-1}$
arc th	$\tanh^{-1}$
arc cth	$\coth^{-1}$
arc sch	$\sech^{-1}$
arc csch	$\csch^{-1}$

---

rot	curl
lg	log

THEORETICAL AND EXPERIMENTAL STUDIES OF THE SHAPED-CHARGE PHENOMENON*

Introduction

Mining engineers knew, in the 1800's, that the force of an explosive charge blast can be concentrated on a small area if the charge is arranged so that there is a cavity (cumulative cavity) in the charge opposite this area. The first mention of the effect of explosive charges with such a cavity appeared at the end of the 18th century.

In the first years of the Second World War, there appeared nearly simultaneously in the armament of all the main combatant countries a large number of new weapons whose operation was based on considerably modified use of the shaped-charge phenomenon. It was found that, when the shaped cavity of the explosive charge is lined with a thin metal cone, it is possible to penetrate armor plate, concrete walls, and other defensive structures with very small explosive weight. Quite frequently, the new explosive charges had the form of conventional artillery shells with metal lined nose cavity. The advantage of such explosive charges over conventional artillery shells was that their penetrating power was practically independent of flight velocity. When penetrating armor plate, the
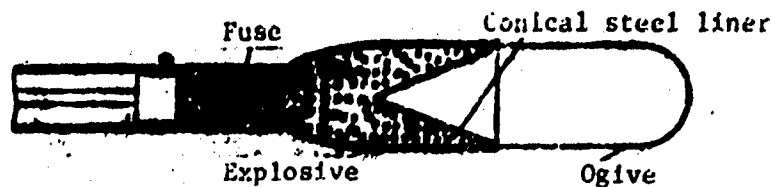
Figure 1. Cross section of head of U.S.A. bazooka showing conical steel liner of shaped explosive charge.

... detonation of such explosive charges was at least as effective as the detonation of the explosive charge of artillery ... which exploded on contact with the target.

This situation forced changes in projectile fabrication techniques, depending on the targets for which they were intended. During the war years, the armed forces of the U.S.A. and Germany used several types of shaped-charge projectiles which were very effective in combatting tanks, in spite of the fact that their flight velocity was much lower than that of the conventional anti-tank artillery projectiles. The American bazooka was used by individual infantrymen. The cross section of the head of this weapon is shown in Figure 1. The missile explodes upon impact of the ogival nose on the tank. As a result of detonation of the explosive charge, the steel conical liner collapses and becomes a high velocity jet which perforates the armor plate and sets fire to the ammunition, gasoline, and oil inside the tank. The German army also had a missile with shaped explosive charge which was used by the infantry against tanks (Faustpatron).

The operating principle and configuration of all these weapons were described briefly in 1945 in [21]. They made it possible for the infantry to combat the largest tanks. The Germans also used weapons with shaped explosive charges and a permanent magnet used to hold the charge against the tank until the time fuse detonated it. Characteristically, the Japanese army used a shaped charge weapon fastened to the end of a long wooden pole. The Japanese soldier charged from ambush with this weapon and jammed it against the tank.
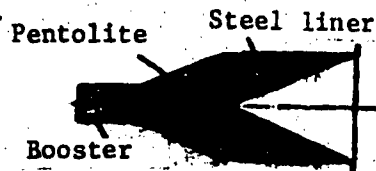
Figure 2. Typical shaped charge with conical steel liner used in static experiments.

Explosive is pentolite (weight 115 g, maximum diameter 41.3 mm, steel liner thickness 0.6 mm).

Since the penetrating ability of these weapons is independent of flight velocity, a large number of experimental studies have been made under static conditions. Figure 2 shows a typical weapon with shaped explosive charge used in the experiments. The conical cavity of this charge has a steel liner. When the detonator is exploded, a detonation wave develops and travels along the axis of the charge and collapses the steel liner cone, starting from its apex. From the collapsing cone, there is formed a long thin steel jet which travels to the right along the extension of the cone axis with a velocity of about 9 km/sec.* The high velocity jet penetrates the armor plate in much the same way as a powerful stream of water from a fire hose forces its way through a mass of soft mud.** The pressures produced by the jet traveling at this high velocity are so much greater than the ultimate strength of the armor plate that the hardness of the latter plays a negligible role in retarding jet penetration through the plate. In fact, mild steel provides nearly as much protection against these weapons as does hard armor steel.

The shaped explosive charge principle may also find application in peaceful pursuits. Of the many suggestions which have been advanced, only a few have proved to be practically feasible, since the same results can be achieved just as well or better in other ways.

---

*Conventional rifle bullets have muzzle velocities of about 600 — 900 m/sec; in the case of special artillery projectiles, the velocity may approach 1.5 km/sec.

**Profound analogies cannot be drawn between these phenomena. While the water stream washes away the mud, the metal jet does not wash away or erode the target metal. Careful weighing shows that the metal jet is captured by the target material, while the target essentially loses no weight (except for a very small amount at the front surface). The hole is formed as a result of radial plastic flow of the target material.

Shaped explosive charges have often been used in demolition work for rapid boring of holes in rock formations. After a hole has been blown with the shaped charge, the cavity can be refilled with explosive for further blasting. This blasting technique is quick and easy, but because of the high cost of the explosive used in shaped charges, it can seldom be justified. The explosives which are used in military operations are needed to obtain satisfactory shaped charge performance, since the performance of the cheaper explosives which create low blasting pressures is definitely inferior.

Charges with lined wedge-shaped cavities are used for cutting cables, bridge beams, and salvage work on sunken ships. Long shaped charges with long cavities with metal wedge-shaped liners can be used for cutting large steel plates of sunken ships with less danger to the workmen than when using oxygen torches. This appears the most practical of the shaped charge applications.

A patent has been issued in the U.S.A. for application of a group of shaped charges to increase oil well production under certain conditions [28]. The charges are lowered into the well and fired so as to form radial holes in the casing tubes and in the surrounding rock to increase oil seepage into the well. This method appears to be superior to the method of cracking the surrounding rock with ordinary explosive charges.

Shaped charges can be used to break up large rocks. They are better for this purpose than other charges. However, recent tests have shown that the effectiveness of breakup of large rocks increases only slightly when a given weight of explosive is formed into a shaped charge.

The shaped charge principle can be used to investigate the properties of various materials subjected to high pressures. Under favorable conditions, such charges produce short-term dynamic pressures concentrated on a small area which are higher than a

4

quarter of a million atmospheres.* By varying the explosive type, cavity shape, and liner material, we can obtain a "graded" sequence of ultrahigh dynamic pressures. The study of phenomena at these high pressures is, of course, associated with severe difficulties. Nevertheless, preliminary experiments have shown the possibility of creating special charges for determining the ultimate stresses in materials at very high strain rates. The data which will be obtained will permit some clarification of the question of the propagation rate of dislocations in metallic crystals and microcracks in glass. There are at least three types of experiments for determining the ultimate shear stresses, so that the results of one type of experiment can be used to check the results of another. In experiments of the first type, we measure the volume and contour of the cavity formed in the target during explosion of the same standard charges. In the experiments of the second type, we measure the depth of the residual penetration of the jet discharged by the standard charge into the material of a standard target such as mild steel after it has perforated a given thickness of the test material. In the experiments of the third type, we measure the velocity of perforation of the jet through the target material. Difficulties are encountered when interpreting the results of these three types of experiments which it is hoped can be eliminated when the phenomena discovered have been studied more thoroughly.

The hollow charge linings can be made from various materials and can have various geometric shapes. Many different forms of liners are used in combat weapons. Charges using hemispherical, paraboloidal, pear-shaped, and trumpet-shaped liners have been tested. Although differences in the performance of weapons with the different liner shapes were observed, none of them had any remarkable advantage in comparison with the others. Hollow charges improvised from headlamps taken from disabled cars have sometimes been used in military operations; the plastic explosive was placed behind the headlamp reflector.

---

*Bridgman measured static pressures on the order of 100,000 atm concentrated on an area 21 x 2 mm and obtained an estimated pressure of 400,000 atm, but was not able to make observations at this high pressure.

Shaped charges with conical cavity and liner intended for penetrating massive targets and explosive charges with wedge-shaped cavities and liners intended for cutting metal are encountered more frequently and have been studied most thoroughly. Each of these liner shapes is very effective in special purpose applications. In the following, we shall investigate explosive charges with cavity and liners of these two types only. Since most of the reliable data have been obtained for charges with conical cavity and liner similar to that shown in Figure 2, the conclusions presented below apply in most cases only to such charges.

The jet formation mechanism was revealed using the flash radiograph method, which permits observing the charge during collapse. Referring to Figure 2, the detonator explosion starts a detonation wave traveling along the axis of the charge. When the wave reaches the apex of the thin steel cone, it suddenly produces a very high pressure on the outside of the cone which causes collapse of the cone walls. The forces which arise are so great that strength of the steel has practically no influence on the phenomenon and the steel can be considered an ideal fluid. The explosive pressure on the outside causes the thin walls of the cone to travel inward nearly perpendicular to the liner surfaces with high velocity. The moving steel liner retains a conical shape with the apex moving along the axis to the right. To the left behind the moving apex, the cone is completely collapsed; the metal there previously belonged only to the outer part of the liner. A jet is formed from the inner part of the cone and is squeezed out of the inner apex of the lining and travels at high velocity along the axis (to the right, in Figure 2). In other words, the metal of the conical liner is divided into two parts by a cone lying somewhere between the inner and outer surfaces. The metal of the outer cone is deformed into a slug which travels to the right (see Figure 2) at relatively slow speed (500 — 1000 m/sec). The metal of the inner cone forms a jet traveling along the axis to the right at very high speed (2000 — 10,000 m/sec). It is this jet which penetrates deeply into the target and produces the damage shown in Figures 3 — 6. It was originally thought that the major part of the damage
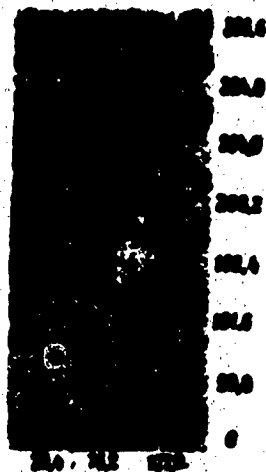
Figure 3. Photograph of solid
steel cylinder (diameter 82.5 mm,
length 178 mm) section.

Charge cross section in position
prior to detonation shown above.
Charge contained 113.5 g of
pentolite; conical cavity was
lined by steel cone 0.6 mm
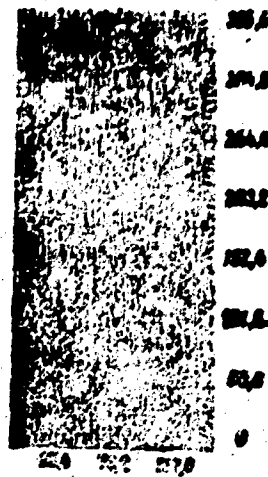thick (base diameter 41.5 mm).

Figure 4. Photograph of solid
lead cylinder (diameter 107
mm, length 240 mm) which was
treated the same as the steel
cylinder in Figure 3.

The steel slug formed from the
conical liner can be seen
embedded in the lead about
127 mm from the base of the
cylinder.

was produced by the slug, but high speed movies make it possible to
clarify the true nature of the phenomenon. This was later con-
firmed by the fact that experiments showed that the slug often
lodges in the middle of the hole made in the thick steel plate by
the jet. Some cases of destruction by shaped charges are shown in
Figures 3 — 6.

Figure 3 is a photograph of the meridional section of a solid
steel cylinder damaged by an explosive charge like that shown in
Figure 2. The shaped charge used to produce the damage is shown at
the top in Figure 3 in the position prior to detonation.

Figure 4 is a photograph of a solid lead cylinder which has
been damaged in the same way as the steel cylinder shown in Figure
3. The hole in the lead is broader and deeper, since the strength
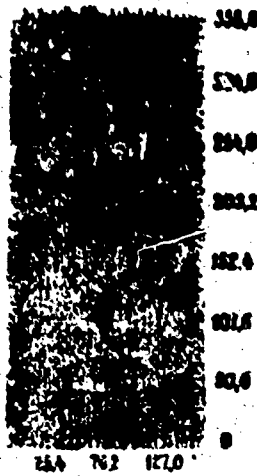of lead is lower and the plastic deformations are larger.

Figure 5. Photograph of laminated cylinder treated similar to the cylinders in Figures 3 and 4.

Upper layer is steel, next is lead, third is steel, and so on. Original layer diameter dimension was 102 x 102 x 12.5 mm. We see clearly in the photograph that the various target elements retain the radial momentum component for a short time after the jet passes through them.

Figure 6. Photograph of lead disc (diameter 203 mm, thickness 51 mm) located 457 mm from charge similar to that shown in Figure 3.

After explosion of the charge, the jet made the through hole and the slug embedded at the top. Evidently, the slug and jet often do not travel in the same direction.

Figure 5 is a photograph of the section of a laminated cylinder consisting of alternating steel and lead plates, which shows the effect on such a cylinder of the shaped charge shown in Figure 2. Figure 5 shows the charge in the position prior to detonation. This picture provides a striking demonstration of the fact that the radial plastic flow produced by the jet is arrested more rapidly in materials with high yield strength (steel, for example) than in materials with low yield strength (lead, for example). The diameter of the jet which made these holes was not over 2 mm, as shown by the flash radiographs. The diameter of each of the holes formed is considerably greater than the jet diameter, even in the steel plates.

Before obtaining radiographic data on the jet dimensions, some interesting experiments were conducted which showed quite conclusively that the jet dimensions must be much smaller than the holes created by the jet. In these experiments, the jet from a shaped charge prior to reaching the target passed through a hole in a
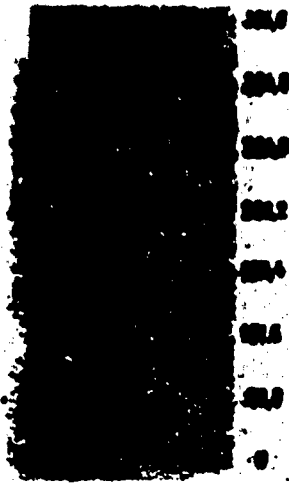
8

Figure 7. Photograph of section of steel cylinder similar to that shown in Figure 3, fractured by charge without steel liner.

steel plate. Although the diameter of the cavity formed by the jet in the steel target was nearly 25 mm, the diameter of the hole through which the jet passed prior to striking the target could be reduced to 6.4 mm without altering the destructive effect. It is suspected that the jet diameter was considerably less than 6.4 mm, since it is known that the jet oscillates somewhat and this increases its apparent diameter.

This charge was exploded in direct contact with the cylinder, since such a charge produces the deepest holes at zero standoff, in contrast with the lined shaped charge, which produces the greatest damage at larger standoff.

Figure 6 shows a picture of a lead disc (5.8 mm thick and 305 mm diameter) in which the large hole was formed by the shaped-charge jet which passed through it. The slug, traveling much slower than the jet, lodged in the disc. The disc was located 45 cm from the charge and this explains the large distance between the holes made by the jet and the slug; because of charge asymmetry, the jet and slug often travel along somewhat different paths.

Figure 7 shows, for comparison, a photograph of a steel cylinder damaged by a charge without metal liner placed on its surface. While lined cavity charges produce deeper penetration when they are placed a short distance from the target, unlined charges produce the deepest penetration when they are in direct contact with the target.

Figure 8 shows the effect produced by a conventional charge without a cavity. This charge obviously contained more explosive than the shaped charge, since it had the same dimensions, but no cavity.
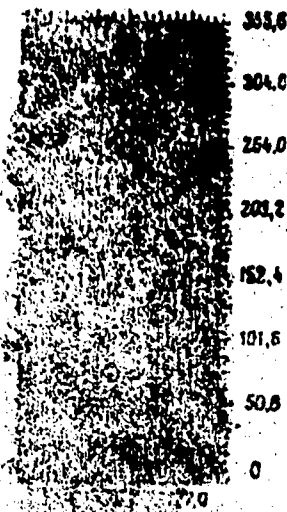
355,6
304,8
254,0
203,2
152,4
101,6
50,8
0

Figure 8. Photograph of section of steel cylinder similar to that shown in Figure 3 after explosion of solid charge.

a
b
c
d

Figure 9. Photographs of hollow charges with metal liner.

In order to better understand the process of cavity liner collapse and jet formation, flash radiography pictures were first taken of charges of relatively small size with 45° conical cavity and steel liner.

Figure 9a shows a picture of one of the charges prior to detonation and Figure 9b shows the charge

a- prior to detonation: explosive charge is cast around a steel liner about 0.05 mm thick with apex angle 45°, charge diameter is the same as that of the base of the cone minus the flange area; b- approximately at the instant when the blast wave reached the apex of the conical shell, i.e., when detonation of the final charge elements began, the metal jet is seen inside the cone; c- 4.8 microseconds after the blast wave reached the base of the cone; d- 22.5 microseconds after the blast wave reached the base of the conical liner. The undisturbed liner flange, metal jet, and the slug are visible.

at the instant the detonation wave has just reached the flange of the 45° conical steel liner. We see clearly the collapse of the liner and its travel toward the axis of the charge. In this picture, we also see the first stage of jet formation at the axis of the charge, since part of the collapsing liner has already reached the axis. Figure 9c shows a later stage of liner collapse, a few microseconds after the explosive has detonated. Figure 9d shows a picture taken about 22 microseconds after all the explosive has detonated; we see the resulting metal jet formed from charges of this type.
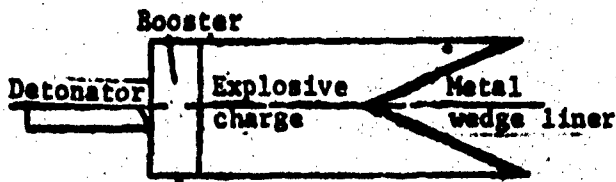
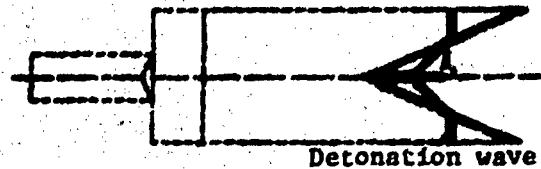Figure 10. Hollow charge with wedge-shaped liner fired by electric detonator.

Figure 11. Collapse of hollow wedge-shaped charge. Detonation wave from primary and secondary detonators has passed through a large part of the liner and collapsed it.

The phenomena described above can be easily understood if we apply some very simple theoretical considerations, which will now be presented.

Theory of Jet Formation in Charges with Conical and Wedge-Shaped Liners

An elementary mathematical explanation of jet formation from conical and wedge-shaped liners can be given. Figure 10 shows the charge cross section; the conical charge is obtained by rotating this section about the axis of symmetry, the wedge-shaped charge is obtained by parallel movement of this section perpendicular to the axis of symmetry. We shall first examine the wedge-shaped charge case. The wedge collapse process is shown in Figure 11. The detonation wave propagating to the right from the booster detonator collapses the liner. The wave creates pressures so great that the strength of the liner material can be neglected and we can consider it an ideal fluid. We assume that, after the liner walls have received the initial impulse from the detonation wave, the pressures on all sides of the walls quickly equalize and the walls continue to collapse inward with no appreciable change of velocity.*

Because of the fact that finite time is required for detonation wave passage from the apex to the base of the liner, the angle 2β between the moving walls will be greater than the angle between the walls of the original liner.

_____

*This assumption is later replaced in view of its inadequacy in explaining the formation of the entire jet.
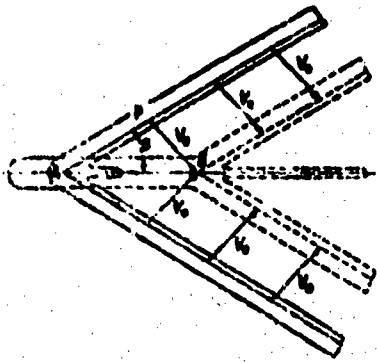
Figure 12. Formation of jet and slug from conical or wedge-shaped liners whose sides collapse with constant velocity V_0 from explosion of a charge which is in contact with the outer surface of the target. Solid lines show liner position at instant of time close to beginning of collapse, dashed lines show position of liner walls after they have traveled a distance equal to V_0.
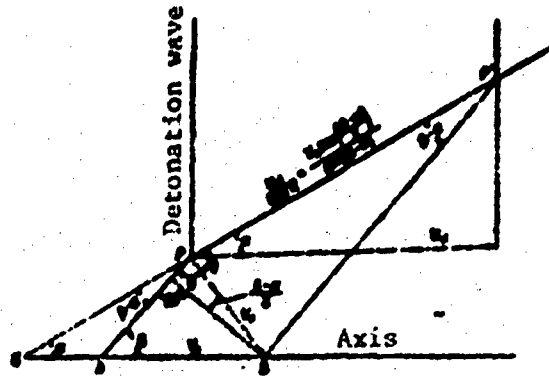
Figure 13. Geometry of collapse process.

OPP' is generator of original cone or wedge; AP is collapsing generator, traveling with the velocity V_0 whose direction bisects the angle APP'. The detonation wave (velocity U_a) moves from P to P' in unit time; after this same time, P'B becomes the collapsing shell; A travels to B at the velocity

$$V_s = V_0 \frac{\sin \frac{\beta-\alpha}{2}}{\sin \beta} = V_0 \frac{\sin \frac{\beta-\alpha}{2}}{\sin \beta}, \text{ since } U_a = \frac{V_0}{\sin \beta}.$$

The effect of the detonation pressure, acting over very short distances, is to give the liner the velocity V_0, whose direction bisects the angle between the perpendicular to the original liner surface and the perpendicular to the collapsing liner surface.*

The walls of the collapsing liner are two planes moving inward as shown in Figure 12. We see from Figure 13 that the junction formed from the liner material near A moves to B with the velocity

*To show that the vector V_0 bisects the angle APP' (see Figure 13), we consider a coordinate system whose origin travels in unit time the distance PP' with constant velocity. In this coordinate system, a steady-state regime exists near the coordinate origin, in spite of the fact that the liner flowing along P'P is forced to curve and flow along PA. This curvature takes place because of the action on the liner of the detonation wave pressure, which is applied at the same place all the time. The liner velocity changes its direction upon passing through the coordinate origin but does not change its magnitude, since the pressure forces are at all times perpendicular to the direction of motion. Let P'P and P'B (parallel to PA) be the liner velocities in the moving system, respectively,
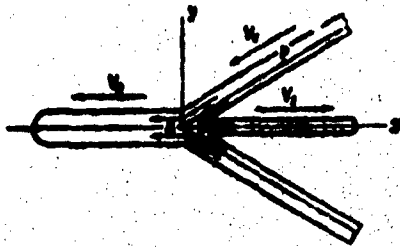
$$V_1 = \left[V_0 \frac{\cos \frac{\gamma - \alpha}{2}}{\sin \beta} \cdots \right].$$

Figure 14. Formation of jet and slug from conical or wedge-shaped liner shown in Figure 11 from viewpoint of observer traveling with the junction A.

For an observer moving with this junction, any point P of the upper plane travels with a velocity equal to the vector difference between the velocity of the walls and the velocity of the junction. The observer sees the point P approaching him with the velocity

$$V_0 - V_0 \frac{\cos \frac{\gamma - \alpha}{2}}{\cdots} + V_0 \cos \frac{\cdots}{2}.$$

Furthermore, as shown in Figure 14, he will see the jet moving off to the right and the slug moving to the left.

We now come to the crucial point of our discussion. As viewed by the observer, the entire process is steady-state and we can use the Bernoulli integral

$$\int \frac{\cdots}{\cdots} + \frac{1}{2} \cdots \qquad (1)$$

If the liner material can be considered incompressible, i.e., $\rho = \rho_0$, we obtain

$$\cdots + \frac{1}{2} \cdots \qquad (1')$$

---

prior to and after passing through the coordinate origin. They are equal in magnitude. Since the velocity of the moving system is represented by the vector P'P, the velocity of the collapsing liner in the stationary system is equal to the vector PP' + P'B = PB = V_0. Since the triangle BPP' is isosceles and P'B is parallel to PA, the angle BPP' is equal to the angle PBP' and the angle BPA. Therefore, V_0 bisects the angle APP'.

13

In both cases, the pressure at a given point of the fluid determines the fluid velocity at this point. We assume that the liner moves away so fast that the pressure on its surface is very low, and hence the pressure is constant on the entire surface of the collapsing liner. It is well known that the pressure, and hence the velocity, are constant at the boundary of the jet. From the viewpoint of our observer, the jet and slug recede with the same speeds V_2 as the walls approach him (see Figure 14). In particular, during liner collapse, the jet and slug have the same length, which is observed experimentally.

In the stationary coordinate system, the jet, traveling to the right in Figure 14, has the velocity

$$V_j = V_0 \left[\ldots \right]$$

while the slug, traveling to the left in the moving coordinate system of Figure 14, actually has a small velocity to the right

$$\blacksquare$$

In order to visualize the entire process, we consider that: if the point P, located on the upper surface in Figure 12, travels to point B, fixed in space, in unit time, the material of the inner part of the upper liner included between PA and AB moves into the jet, whose front moves during this time to the right a distance equal to PA + AB. Thus, the high velocity jet which penetrates deep into the target is formed from the liner material. Its velocity is

$$V_j = V_0 \left[\frac{}{} + \frac{}{} + \frac{}{} \right]. \tag{2}$$

the material of the outer part of the liner surface forms a slug which travels with relatively low velocity

$$V = V_0 \left[\frac{}{} - \frac{}{} - \frac{}{} \right]. \tag{3}$$

With the aid of the momentum theorem, we can determine the liner mass division between the jet and the slug. Let m be the mass per unit length of the two collapsing planes which come together at the junction. Let m_j be the part of m going into the jet, and m_s — the part going into the slug; thus, $m = m_j + m_s$. The horizontal component of the momentum prior to and after splitting of m between the jet and the slug must be the same; hence we have, in the moving coordinate system (Figure 14),

$$m(V_0) - V_0 \frac{}{} = V_0$$

hence

$$m_j = \frac{m(1 - \cos\beta)}{2}$$
$$m_s = \frac{m(1 + \cos\beta)}{2}$$

$$(-)$$

Thus, the velocities and cross sections of the jet and slug are constant.

The conical liner case can be treated in the same way. However, in this case, the problem will have an axis of symmetry rather than a plane of symmetry and the material from the collapsing liner will converge to the junction from all sides of this axis. In this case, the moving observer can be selected just as in the wedge case. However, in order for the entire process to appear stationary to this observer, it is necessary that the mass per unit axis length be constant. This requirement is satisfied only approximately for the liner of constant thickness and is satisfied exactly for a liner whose thickness is inversely proportional to the distance from the apex.

In the case of a plane detonation wave traveling along the axis with the constant velocity U_d, we can compute V_0 exactly from the basic relation

$$U_d = \frac{V_0 \cos \frac{\alpha}{2}}{\sin(\beta - \alpha)}.$$

which follows from purely geometric considerations (see Figure 13).

Substituting the value of V_0 obtained from this relation into
(2) — (3), we obtain

$$V_j = U_d \frac{\sin(\beta - \alpha)}{\cos\alpha} \left(\cos\beta + \operatorname{ctg}\beta + \operatorname{tg}\frac{\beta - \alpha}{2} \right). \tag{2'}$$

$$V_s = U_d \frac{\sin(\beta - \alpha)}{\cos\alpha} \left(\cos\beta - \operatorname{ctg}\beta - \operatorname{tg}\frac{\beta - \alpha}{2} \right). \tag{3'}$$

The jet velocity increases as the angle α decreases, since, in this
case, the angle β also decreases. In the plane detonation wave case,
the jet velocity approaches the maximal value as α approaches zero.
From (2') for $\alpha = 0$, we have $V = 2U_d$, i.e., *the jet velocity cannot
exceed twice the detonation wave velocity.*

In the hypothetical case of a conical wave front traveling
perpendicular to the surface of the conical liner so that it strikes
the entire liner surface at the same instant, $\beta = \alpha$ and we obtain
from (2) and (3) the simple formulas for the jet and slug velocities

$$V_j = \frac{V_0}{\sin\alpha} (1 + \cos\alpha).$$

$$V_s = \frac{V_0}{\sin\alpha} (1 - \cos\alpha).$$

In this case, *the jet velocity increases without limit with
reduction of the cone angle.* However, as α tends to zero, the jet
mass

$$m_j = \frac{m}{2} (1 - \cos\alpha)$$

and the jet momentum

$$m_j V_j = \frac{mV_0}{2} \sin\alpha$$

also tend to zero.

Thus, we have determined theoretically the jet and slug
velocities [(2) — (3) and (2') — (3')] and their masses (4) for
both conical and wedge-shaped liners.

Comparison with Experiment and Further Remarks

The preceding theoretical arguments correspond roughly to experiment with important exceptions. Flash radiographs show that the angle 2β of the collapsing cone is greater than the original cone angle and remains approximately constant throughout the collapse process, which is in complete agreement with the theory. Further, the radiograph data and some other measurements show that the speed of the steel jet front and slug are close to the speeds predicted by (2) and (3); but contrary to the theory predictions, the speed of the rear or last-formed parts of the jet is considerably slower than that of the front parts. Also contrary to the theory predictions, the jet is emitted even after the liner has collapsed completely.

Since the angle β can be determined approximately by flash radiography, (4) can be checked experimentally if either the steel jet or the slug can be recovered from the target after the explosion. This can be done with both the jet and the slug, but it is more convenient and easier to deal with the slug.

During explosions of charges with wedge-shaped cavities and liners, slugs which survive the detonation and subsequent collapse process are not formed; however, during explosions of charges with conical liners with apex angles of 60° and less, such slugs are formed. If the charge is exploded in sawdust or water, these slugs can be recovered from the target virtually undamaged. It has been found that a smaller part of the conical shell mass than predicted by the theory (see [4]) goes into the formation of these slugs. This is not surprising, since even qualitative studies of the slug show that the cone collapse process does not remain at all times ideal as was assumed in deriving (4). If, prior to loading and firing, the charge conical liner is sectioned by a series of planes parallel to the base, the jet from such a charge will be formed normally and will have the usual performance. Each section of the cone forms a corresponding portion of the slug. These portions, recovered from the target in the form of individual pieces

17

and fitted together, form the same slug as that formed in the usual way. By weighing each part of the liner before and after firing, we can determine what fraction of the liner enters the slug and what part enters the jet. It was found that, for the parts of the cone close to the apex, the distribution of mass between the jet and the slug agrees with (4) within the experimental uncertainty in determining β from the radiograms. The percentage weight loss increases for the parts of the cone located near the base. This may be due, in part, to incomplete cone collapse near the base and breaking off of some metal, and also to the formation of an afterjet from the slug after the collapse process is complete. The formation of the afterjet from the slug is also clearly seen from the radiogram data.

It would be interesting to establish why jet formation continues for some time after completion of the collapse process. It may be that the pressure of the detonation wave in the gaseous explosion products concentrates near the slug and squirts the afterjet out of it like toothpaste is forced from a tube. Studies of slugs recovered from the target have shown that the metal temperature near the slug axis is close to the melting point. The detonation wave pressure which may converge on the newly formed slug undoubtedly coincides with the pressure which would be created by explosion of the same charge without a liner. Immediately after a hollow charge without a liner has been exploded, the compressed gases stream into the cavity and converge on the axis, forming a high velocity jet.* The effect produced by such a charge is shown in Figure 7.

In order to explain the observed afterjet velocity using this scheme, it is necessary that the secondary compression wave converging on the slug create a higher pressure than that which we would expect from the explosion of a charge similar to that shown in Figure 2. Therefore, some other explanation must be found.

---

*Similar to jet formation behind an ordinary sphere dropped into water [30].

18

Another possible explanation of afterjet formation is that
it is pulled out from those parts of the original jet which are
immediately adjacent to the slug throughout the entire jet forma-
tion process. This ductile drawing process can be compared with
filament formation from molten glass or quartz. Experiments carried
out by Bridgman showed that most metals become very plastic under
the influence of high pressure. It may be that the metal does not
lose this property for a few microseconds after the pressure is
released. If this latter mechanism is correct, it would account
for the velocity gradient existing in the jet, since acceleration
of the slug material causes deceleration of parts of the jet already
formed. The latter mechanism is more probable than the preceding,
but it is possible that both mechanisms play some role.

The afterjet forms especially easily because the core of the
slug is heated almost to the melting point. This heating may be
explained by the following crude approximate two-dimensional theory
of propagation of the heat caused by deformation of the liner (the
time involved in heat propagation is too short for heat conduction
to be important).

Let us again introduce the moving coordinate system of Figure
14 and assume that the linear material deforms as a perfect fluid
[30]. Let u and v be the components of velocity along the x and y
axes, respectively, at the point with coordinates (x, y). We know
from classical hydrodynamics that the divergence and curl of the
velocity vector are equal to zero, i.e., u and v satisfy the Cauchy-
Riemann conditions

$$\frac{\partial u}{\partial x} = -\frac{\partial v}{\partial y}, \qquad \frac{\partial u}{\partial y} = -\frac{\partial v}{\partial x}.$$

Hence, the infinitesimal strain tensor [31] is described by the
matrix

$$\begin{vmatrix} 1+a & b \\ b & 1-a \end{vmatrix}.$$

characteristic roots may be written as

$$\lambda = 1 \pm \sqrt{a^2 + \bar a \cdot a} = 1 \pm \left|\frac{a}{2}\right| a.$$

where $\zeta = u - iv$ is the conjugate complex velocity and $z = x + iy$ is the complex position vector. Hence, the rate of strain of a given infinitesimal fluid element is proportional to $\left|\frac{\zeta}{z}\right|$.

For simplicity, let us assume that the heat of deformation of this element depends only on its total strain

$$\int \left|\frac{\zeta}{z}\right| dt$$

and is independent of the rate of strain. The integral is evaluated for the element as it travels through the region near the stagnation point. Then

$$\int \left|\frac{\zeta}{z}\right| dt = \int \left|\frac{dt}{dz}\right| \left|\frac{\zeta}{z}\right| dz$$

But

$$\left|\frac{\zeta}{z}\right| = \frac{1}{\left|\frac{dz}{dt}\right|}$$

Hence, the heat generated by each of the elements is proportional to

$$\int \left|\frac{\zeta}{z}\right| dt = \int \frac{1}{\left|\zeta\right|} \left|\frac{\zeta}{z}\right| dz = \int \frac{d\zeta}{\zeta} = \log \zeta \tag{5}$$

That is, the total heat referred to unit volume is proportional to the variation of the logarithm of ζ or the logarithm of the complex velocity $\zeta = u + iv$. Since the logarithm of zero is infinite, it is clear that the elements near the axis of the jet which pass near the stagnation point may be heated infinitely strongly. Possibly, as the temperature of the liner material approaches its melting point, the properties of the material approach more and more the properties of the ideal fluid with negligible viscosity, so that the heating is reduced greatly and, as a result of this, only a very small part of the metal is melted.

20

Jet Penetration into Target

The process of hollow charge jet penetration into a target is much like that of a high speed jet from a fire hose penetrating a bank of soft mud. Target material is splashed out radially at high velocity from the impact point. The diameter of the hole produced is considerably greater than the jet diameter and is not directly related to this diameter. It depends, rather, on the jet energy per unit penetration depth (see [32], where proportionality between the impact energy and the hole or crater volume is proved experimentally). As shown in Figures 3 — 5, the hole diameters in hard materials are less than in soft, since more work must be expended in destruction of the hard material. In soft materials like lead, large diameter holes are produced because the material spreads radially from the point of collision with the jet until it is stopped by elastic forces or viscous forces.

On the other hand, for most charges, the rate and depth of penetration into the target are nearly independent of the target material strength. This arises from the fact that, because of the high velocities, the shaped-charge jets create at the impact point pressures which exceed markedly the yield point of most materials. To a first approximation, the strength and viscosity of the target material can be neglected and we can solve the problem on the basis of the laws of hydrodynamics.

Target Penetration by Constant Velocity Jet

Consider a jet of constant length l, velocity V_j, and density ρ_j (Figure 15a) penetrating a semi-infinite target of density ρ_t with the velocity U (see Figure 15b). We consider the case when U remains constant. The phenomenon simplifies if it is examined in a coordinate system moving with the velocity U (see Figure 15c). In this coordinate system, the hole profile is fixed and the jet travels to the right at the velocity $V_j - U$, while the target moves
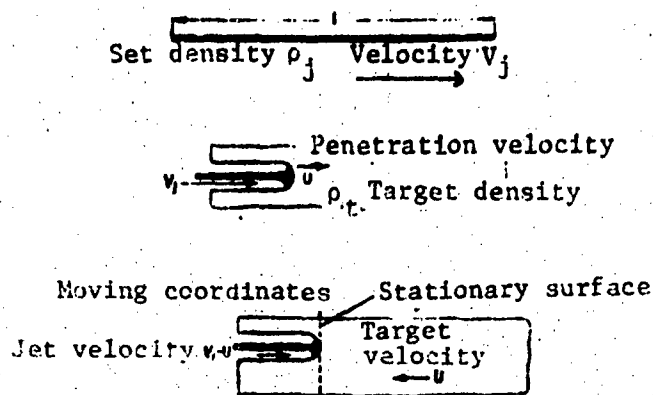
Figure 15. a- idealized jet of length l with velocity V_j, density ρ_j, and cross section area A; b- idealized jet penetrating target material of density ρ_t with velocity U. Since the jet is continuous, it spreads out as it reaches the target; c- steady state (b) in coordinate system traveling with penetration velocity U. In this moving coordinate system, the hole contour is fixed.

to the left at the velocity U. If the jet pressure is larger than the strengths of the jet and target materials, the latter can be treated as ideal fluids. The pressure on the two sides of the jet and target contact surface must be the same. From the Bournelli integral, which can be used since the phenomenon is stationary in the coordinate system, we have selected

$$\tfrac{1}{2}\rho_j(V_j - U)^2 = \tfrac{1}{2}\rho_t U^2. \qquad (6)$$

The velocity U has been measured for a large number of charges and target materials. When using charges of the type shown in Figure 2, the velocity U in the steel target case was on the order of $2.7 \cdot 10^5$ cm/sec. In this case, the jet pressure is $(1/2)\rho_t U^2 = 0.5 \times 7.8$ $(2.7 \cdot 10^5)^2 = 2.8 \cdot 10^{11}$ dynes/cm^2 or more than a quarter million atmospheres, which exceeds by far the yield strength of any steel and hence, confirms the possibility of using the methods of hydrodynamics.

The mechanism of jet penetration into the target is illustrated in Figure 14, which shows how the jet interacts with the target. If it is assumed that the steady state is reached nearly instantaneously and that the penetration stops as soon as the end of the jet reaches the target,* the total penetration on the basis of (6) will be

$$P = U t_j = \frac{Ul}{V_j - U} = l\left(\frac{\rho_f}{\rho_t}\right)^{\frac{1}{2}}. \tag{7}$$

where l is the original jet length and t_j is the penetration time.

This indicates that the depth of penetration into a massive target depends only on the length and density of the jet and the target density and not on the jet velocity. At first, this seems surprising. However, upon careful examination, we see that the jet penetration velocity [see (6)] and the rate at which the jet is dissipated are proportional to V_j. Hence, we see that, the faster the jet travels, the faster it is dissipated and thus the total penetration depth does not change as a function of the velocity V_j. Of course, this independence of the depth of penetration on the jet velocity can hold only for velocities at which the pressure generated exceeds by far the yield strength of the target material.**

We see from (7) that the penetration depth of the jet from a given charge should be inversely proportional to the square root of the target material density. This agrees very roughly in many cases with experiment, but there are many exceptions for which this rule must be modified.

---

*It is probable that, when the jet strikes a relatively soft target, all the jet momentum is not expended and the hole in the target will be made deeper as a result of the residual momentum. We term this effect secondary penetration; it is not considered in (7). This explains the fact that the hole depth is greater in a massive lead target than in a massive steel target, even though lead has the higher density.

**In the case of a jet formed from a conical liner, a small amount of the liner material travels behind the jet so slowly that it does not form a pressure greater than the yield strength of armor steel but sufficiently fast to exceed the yield strength of mild steel. Thus, the process of penetration into mild steel lasts longer than the process of penetration into armor steel. This phenomenon,
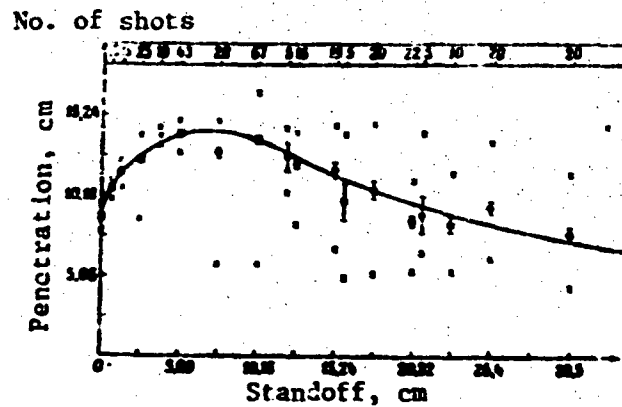
No. of shots

Figure 16. Curve of average penetration into mild steel as a function of standoff for standard charge.

○- average penetration with average mean deviation; x- maximal and minimal penetrations.

This theory explains correctly a number of experimental phenomena, but at the same time, there are many experiments which do not correspond to this simple jet theory. With increase of the distance between the charge and the target, the average penetration into a given target at first increases and then decreases (see Figure 16; a charge of the type shown in Figure 2 was fired into a mild steel target).

A number of tests have been conducted in which the massive mild steel target was part of a ballistic pendulum, so that the momentum of the jet could be measured simultaneously with the penetration it produced. These experiments showed that, while the average penetration depth varied greatly with standoff, the average momentum was almost constant. This result agrees well with the present theory, which indicates that the penetration should be independent of the jet velocity. Confirmation of this is found in Figure 17, where the abscissa axis is the penetration depth and the ordinate axis is the corresponding momentum for the same standoff distance. The maximal momentum changes are less than the maximal

together with the secondary penetration phenomenon (see preceding footnote) accounts for the fact that the total penetration depth into armor steel is less than into mild steel, and that the penetration depth into mild steel is less than into lead.
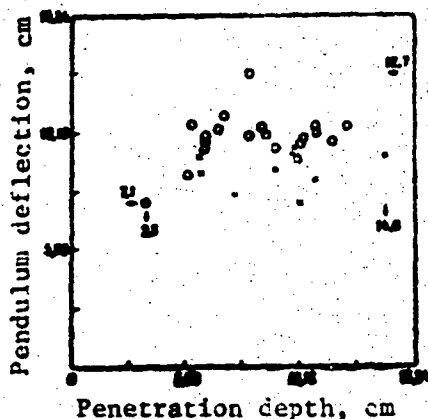
Figure 17. Deflections of ballistic pendulum versus penetrations into mild steel for standard charges at stand-off 305 mm.

Circles show data obtained for charges of one batch; crosses show data obtained for charges of another batch. These charges were made to be identical and observations before firing showed no variations. The charges of the second batch gave nearly the same average penetrations as the first, although the average momentum of their jets was lower.

penetration depth changes, but there is no correlation between the momentum and penetration deviations. Jets having the largest momenta do not produce the deepest penetrations.

If the jet is broken up into very small particles so that they cannot influence one another, the pressure produced by the jet will be greater than that indicated by the Bernoulli integral (6). This is explained by the fact that the particle jet does not spread out over such a large area as the continuous jet. The continuous jet is capable of supporting internal pressure while the particle jet is not. A pressure gardient is created along the jet axis which varies from the maximal value at the point of impact with the target to zero at the other end of the jet. The pressure gradient causes a gradient of the opposite sign in the velocities within the jet from the velocity U at the impact point to V_j at the opposite end of the jet. After the jet begins to travel uniformly, the product of the velocity by the jet cross section area must be the same for all points of the jet; therefore, the jet cross section area increases as it approaches the target.

If we assume that, in the particle jet case, the particles regain their velocity and cross section prior to inelastic impact with the target, such spreading will not take place. The pressure produced by a particle jet can be calculated approximately by dividing the total force required to alter the jet momentum during

impact by the area A of jet contact with the target. The total force is given by the rate of change of the momentum $\rho_j A (V_j - U)^2$ and so the average pressure on the contact surface is $\rho_j (V_j - U)^2$. If this pressure is equated to the pressure formed in the target material at the point of impact and given by the Bernoulli integral (1'), we obtain

$$\rho_j (V_j - U)^2 = \tfrac{1}{2} \rho_t U^2. \tag{8}$$

This relation differs from (6) only by the factor 1/2. The relations (6) and (8) can be combined into one

$$\lambda \rho_j (V_j - U)^2 = \rho_t U^2, \tag{9}$$

where the constant λ is equal to one for a continuous jet, and two for a particle jet. If the jet has an intermediate structure, λ will lie between one and two.

From (9), we can calculate the target penetration depth for a jet of either type

$$P = l \left(\frac{\lambda \rho_j}{\rho_t} \right)^{\tfrac{1}{2}} \tag{10}$$

This formula is valid only for an idealized jet whose properties remain unchanged in the target penetration process. The real jet behaves much more complexly.

Target Penetration by Variable Velocity Jet

Jets formed from a conical liner are not constant but change as they travel. For these jets, (10) must be modified. As mentioned earlier, the jet velocity decreases continually from front to rear of the jet; hence, the jet becomes longer. The increasing jet length leads to change of other jet characteristics in the course of time. Furthermore, at each given moment of time, the jet properties are not the same along its length and usually the jets are not

completely formed at the moment of jet contact with the target. Thus, a question arises: can the target influence the jet in the sense of changing its characteristics during jet formation?

Such influence of the target on jet formation cannot take place if the speed of sound in the jet material is so low that a pressure pulse produced by the target cannot travel back to the vicinity of the stagnation point (Figure 12). This condition is usually realized, even at low standoffs, since the velocities of the front part of the jet are higher and the velocities of the rear part of the jet are, in turn, only slightly lower than the speed of sound in the jet material. With charges of the type shown in Figure 2, the steel target will not have any influence on jet formation if the standoff distance is not less than 12.7 mm. This makes it possible to separate the process of jet penetration into the target from the jet formation process.

To calculate jet penetration into a target, we need to know the physical characteristics at all points of the jet at every instant of time. The exact characteristics are undoubtedly very complex. However, in calculating jet penetration into a target, we need know only the average density ρ_j and degree of dispersion, characterized by the quantity λ, of that part of the jet which strikes the target at a given instant of time. The average density ρ_j is equal to the mass of an elementary volume of the jet divided by the volume. We shall consider that, for a continuous jet, it is equal to the density of the liner material and less than the value for the particle jet. The quantity λ can be considered a function of ρ_j, although it also depends in part on the size of the particles into which the jet is broken. We assume that *the λ and ρ_j for that part of the jet from a given charge which strikes the target at a given instant of time are independent of time and depend only on the distance from the base of the original cone to the target point at which the jet impacts.*

These assumptions are made only to simplify the calculations; they are probably just as valid as any other simple assumptions which could be made. If we neglect the slight compressibility of the liner material, then all parts of the jet of a given charge must leave the stagnation point (Figure 11) with the same density. If the jet, because of the large velocity gradient, breaks up into particles, it is possible that the front part of the jet breaks up first and the rear part later and thus, the entire jet may break up at the same point of space. The change of jet density taking place because of its breakup as a consequence of the existence of the velocity gradient and other causes probably depends more on the distance traveled by the given section of the jet after its formation than on the position in the jet or the time since the process started.

It should be noticed that, while the theory of jet formation from a conical liner of uniform thickness indicates that the mass per unit length in the rear part of each jet should be greater than in the front of the jet, there is no reason to believe that the densities in these parts of the jet will be different. The jet cross section probably decreases along its length from the rear toward the front; this will not influence the depth of jet penetration into the target, but should affect the diameter of the hole produced.

Under these assumptions, since λ depends on ρ_j, the ρ_j (and, hence the λ) for the part of the jet from a given charge striking the target will depend on the distance s of the target from the base of the original cone, but will not depend on t.

We have the formula for the penetration depth

$$P = \int U dt.$$

where the integral is evaluated in the limits from beginning of penetration to the end of jet penetration into the target. But $dZ = (V_j - U)dt$, where dZ is the jet element striking the target, i.e., the element which, during the time dt, will be carried by the

28

jet through the boundary of the target. Hence, neglecting transient
unsteady effects like those mentioned in footnote preceding (7),
we obtain

$$P = \int \frac{v a}{v_t} \, .$$

(11)

where the integral is taken over the entire length of the jet as it
strikes the target. Assuming that (9) holds approximately for the
variable jet, we can rewrite (11) as follows

$$P = \int \left(\frac{u}{\rho_t} \right)^2 a$$

(12)

or, if the target has constant density,

$$P = \frac{1}{\rho_t} \int u \, a$$

(13)

The integral in (13) depends primarily on the jet characteristics,
so that the penetration depth of variable jets from similar charges
into different targets should be inversely proportional to the
square root of the target density; this is valid for constant jets
as well. However, we see from (13) that the penetration of a vari-
able jet into a given target will depend on the standoff, while the
penetration of the constant jet is independent of this distance.

Let s be the distance between the base of the original cone
and the target surface. Since the jet lengthens as it travels, the
integral in (13) depends for a given jet on s. Exact calculation
of this dependence is very complex and is hardly justified consider-
ing the uncertainty of the original assumptions. However, an
excellent idea of this dependence can be obtained by use of some
approximations.

We write (13) in the form

$$P = J \frac{1}{\rho_t} \int a.$$

where $\bar{J}$ is the average value of ω_j^2 during penetration. This quantity lies somewhere between the values of ω_j^2 at the beginning and end of penetration. According to the assumption that λ and σ for a given charge depend on s but not on time, $\bar{J}$ depends primarily on s.* The integral $\int dl$ also depends primarily on s. If the jet has constant length, $\int dl$ yields the jet length, since integration is made over all the jet elements striking the target. For jets of variable length, $\int dl$ yields the effective length, since it is the sum of the lengths of all those jet elements which penetrate the target. The effective length $\int dl = \bar{l}$ depends primarily on s. Relation (13) is rewritten as follows

$$P = \bar{J}\bar{l}\,\frac{1}{\rho_t}$$
(14)

We can obtain the approximate dependence of P on s from (14).

We shall consider three cases, each of which may be encountered at some stage of penetration of a particular jet into a target.

Case 1. The metal jet is drawn out plastically and becomes narrower. The jet density ρ_j does not change and since λ is constant for a continuous jet and equal to one, P increases in proportion to $\bar{l}$.**

---

*The quantities $\bar{J}$ and $\int dl$ depend weakly on the target density ρ_t, since although penetration into targets with different densities does change the average value of ω_j^2 as well as the value of $\int dl$, this change is so slight that it may be neglected.

**The process of ductile drawing of the jet due to the velocity gradient in it was first suggested because the increase in penetration proportional to ω_j^2 for particle jets (as in Case 3) did not appear to be rapid enough to account for the experimental observations.

Case 2. The jet is in the process of changing from the first to the second type. It has broken up into particles but the particles are still so close together that the impact of the jet on the target is nearly the same as in the continuous jet case. The value of λ lies between one and two, but approaches two in an unknown manner as the jet lengthens. Thus, λ increases with standoff and ρ_J decreases. The average value of $\lambda\rho_J$, denoted by $\bar{J}$, varies, depending on the rate of increase of λ and decrease of ρ_J. If λ increases at the same rate as ρ_J decreases, then $\bar{J}$ remains constant; if λ increases at a higher rate than ρ_J decreases, then $\bar{J}$ increases and, finally, if λ increases at a lower rate than ρ_J decreases, then $\bar{J}$ decreases. Some experiments suggest that $\bar{J}$ first increases slightly and then decreases with increasing standoff. Probably the penetration produced is much the same as that of Case 1, when $\bar{J}$ is constant and the penetration is proportional to $\bar{l}$.

Case 3. The jet consists of finely divided particles with unchanging cross section. The factor λ is constant and equal to two. Since the decrease in ρ_J is caused by lengthening of the jet due to its velocity gradient, the average value of ρ_J should be inversely proportional to $\bar{l}$, and $\bar{J}$ should be inversely proportional to $(\bar{l})^2$. Thus, from (14), the quantity P will be proportional to $(\bar{l})^{2/3}$ (see preceding footnote). The penetration depth will increase more slowly with increase of the standoff than in Cases 1 and 2.

The nature of the jet from the conical liner depends on the physical properties of the cone material and on the temperature and pressure in the jet. Probably all metallic jets pass through each of these three stages, starting out as continuous jets but, sooner or later, breaking up into particles. Under these conditions, jets of less ductile metal break up into particles sooner than jets of more ductile metal. Thus, charges with liners of a more ductile metal such as aluminum or copper penetrate the target more deeply than charges with liners of less ductile metal. In each case, the

penetrating ability increases with increase of the standoff distance, rapidly at first during stretching of the jet, and then slowly after the jet has broken up into particles. It might seem that the penetrating power of the jets should increase indefinitely; however, this naturally is not so, because:

1.   In practice, the jets are never perfectly uniform, so they tend to spread and their effective density decreases and the penetrating ability decreases.

2.   The density reduction caused by lengthening and spreading eventually reduces the pressure of the jet on the target until the target strength can no longer be neglected and the simplified theory becomes invalid.

3.   The particle scatter upon breakup of the jet is so great that the air resistance for each individual particle becomes an important factor.*

All this reduces the penetrating power with increase of the standoff. Thus, the penetrating ability of a jet formed from a conical liner initially increases at low standoff because the jet first stretches and then breaks down into particles, and then the penetrating ability decreases with increasing standoff, because of the reduction in jet density resulting from its spreading. If we plot the dependence of P on the distance s, the curve rises to a maximum at the optimal standoff and then falls off again as shown in Figure 16. We note that, although the individual points have considerable scatter, the average penetration depth curve is quite smooth. The large point scatter for most charges is associated with imperfect alignment.

---

*At distances of 10 or 15 diameters from the base of the cone, the air can be treated approximately like any other target having the density of air. The front of the jet creates a very intense shock wave with an evacuated space behind it, which reduces the air resistance on the rest of the particles to a negligibly small quantity.

Theory of Jet Penetration into Target

In the variable jet case, an approximate relation for determining the penetration depth as a function of s can be obtained from (14). It is necessary to neglect any changes in velocity caused by the internal forces acting on each of the jet particles in the time interval from jet formation to particle impact on the target.*

The effective jet length l increases linearly with increase of s, since it is known that the velocity gradient along the jet is approximately constant. The ratio of the effective length at standoff s to the length at s = 0 will be roughly

$$1 + k_1 s$$

where k_1 is a constant depending on the velocity gradient.

For particle jets, the effective jet density ρ_j depends on its effective length l and effective cross section area. The effective cross section area of the jet increases with standoff s because of spreading. If large forces do not act on the jet particles, they will travel in a straight line and the radial spreading will depend linearly on s. If the radial spreading is symmetric about the axis, the ratio of the effective jet radius a at standoff s to the jet radius at s = 0 is roughly

$$1 + k_2 s$$

where k_2 is a constant determining the spreading rate. The ratio of the effective cross section area at standoff s to that at s = 0, if the spreading is symmetric, will be

$$(1 + k_2 s)^2$$

---

*This simplification is not serious because the forces acting on the jet particles in this period are relatively small. The internal forces acting during the ductile drawing process change the velocities somewhat, but not enough to seriously affect the rate at which the length of the jet changes, which is what we are interested in.

If the spreading is somewhat asymmetric, this relation holds less exactly.

Although in our study the actual jet density for the continuous jet is constant (Case 1), the effective density may decrease with increase of standoff s because of waver caused by faulty alignment. For lack of reliable data on jet waver, we may assume that the continuous jets waver through the same solid angle as the particle jets spread. The ratio of the effective jet density due to spreading or wavering at standoff s to that at s = 0 is roughly

$$\frac{1}{1+k_1 s}$$

The penetration of these jets can now be calculated approximately from (14). For Cases 1 and 2, we have

$$P = P_0 \frac{1+k_1 s}{1+k_2 s}. \tag{15}$$

where P_0 is the penetration at s = 0. For particle jets (Case 3), for which $\lambda = 2$, the penetration is roughly

$$P = P_1 \frac{(1+k_2 s)^2}{1+k_2 s}. \tag{16}$$

where P_1 is the value of P obtained from (15) for $s = s_1$ (s_1 is the distance at which the jet breaks into particles). Generally, each jet passes, in succession, through the stages described by Cases 1, 2, and 3.

Curves of penetration versus standoff can be plotted using (15) and (16) with the values of k_1, k_2, and s_1 determined from other experiments. However, these curves cannot be plotted on the basis of (16) alone. At low standoff, the experimental penetration increases with standoff so rapidly that it is necessary to postulate ductile drawing of the jet to explain this phenomenon.

34

Experimental Studies of Relations for Determining Velocity

Equation (9) indicates that the penetration velocity U depends only on the target material density ρ_t and does not depend on all the other target properties. Since (9) was obtained for a steady-state process like that shown in Figure 15c, it cannot be strictly true for variable jets. However, from it we can obtain the approximate average values of V_j and U, if we measure the velocity over short segments on which the jet properties vary only slightly during the entire process. In comparing the results with different targets, we must locate the targets at the same distance from standard charges so that, as nearly as possible, the average density of the penetrating jet will be the same for each target.

Many studies have been made with targets in the form of plates 51 mm thick of different materials, using standard charges with conical steel liner (cone base diameter 41.5 mm, apex angle 45°, liner thickness 0.9 mm) and standoff 152 mm. A high speed rotating drum camera was used to record the speed just before and just after target penetration (V_{jb} and V_{ja}, respectively) and the time required for penetration. The average jet penetration velocity $\bar{U}$ during the perforation time is

$$\bar{U} \approx \frac{V_{jb} + V_{ja}}{2}.$$

Relation (9) can be written as

$$\frac{V_j}{U} - 1 = \sqrt{\frac{\rho_t}{\rho_j}} - \frac{V\overline{\rho_t}}{j}$$

or

$$\beta = \frac{V\overline{\rho_t}}{j}$$ (17)

where β depends only on the jet density for a given liner material.
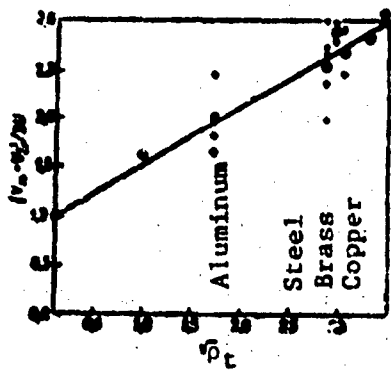
35

Figure 18. Ratio of average jet velocity to average penetration velocity in targets of various materials for standard charges.

Crosses show results of individual tests; circles are averaged results for each material.

If the ratio

$$\frac{v_0 + v_p}{2v_p}$$

of the average velocity is considered a function of $\sqrt{\rho_t}$, where ρ_t is the target density, then (17) is represented by a straight line (see Figure 18). The scatter of the individual points in the figure is quite large, but the points (circles) corresponding to the averages for each of the targets lie fairly close to a straight line, which as would be expected from (17), passes through the point (0, 1).

The scatter of the individual points is due to the variation of the jet density caused by variation of the spreading or rate of elongation of the jet. The jet spreading variations are known to play the primary role. At a distance of 15 — 20 cm from the base of the cone, we can find the average value of $\lambda \rho_j$ (reciprocal of the square of the slope) from the slope of the straight line in Figure 17. The average, maximal, and minimal values of $\lambda \rho_j$ from Figure 17 are, respectively, 3.0, 9.0, and 1.4 g/cm³. If λ is near 2 in each case, the jet density is equal to 1.5, 4.5, and 0.7 g/cm³, respectively. These density values should be compared with the density of steel, equal to 7.8 g/cm³. The value 4.5 g/cm³ is closest to the density of steel and it is likely that this jet acted like a continuous jet with λ less than 2. In this case, the actual density is greater than 4.5 g/cm³.

An interesting effect was noted in some earlier measurements of jet velocities from charges of nearly identical shape before and after they perforated a given target plate. When the target was located near the charge, the jet velocity after perforation

was less than when the charge was located at a greater distance
from the target. For charges of the type shown in Figure 2 but with
an aluminum liner, the velocity after perforating a mild steel plate
51 mm thick at 152 mm standoff was only 4600 m/sec, whereas in the
same experiment with standoff 458 mm, the velocity was 6300 m/sec.
At 762 mm standoff, the velocity again falls to 6000 m/sec.

This rise and fall of the jet velocity after perforating a
given plate may seem surprising at first, although such behavior
of the velocity should be expected on the basis of the discussion
above. The velocity is measured at the front of the jet. The
target shortens the jet by removing the faster particles from its
front. At exit from the plate, the jet consists of slower moving
particles and the observed velocity is slower. The reduction of
the observed jet velocity after plate perforation depends on the
amount of material which the target removes from the front of the
jet. The more jet material removed by the target, the greater is
the reduction in the observed velocity. At both large and small
standoffs, jet penetration into the target is inefficient, since
the major part of its mass is removed by the target, whereas at
optimal standoff, the jet penetration is most efficient; in this
case, the smallest amount of material is removed. Since the velocity
gradient is nearly constant along the length of the jet, the amount
of jet material removed is roughly equal to

$$\frac{\Delta V_j}{V_A - V_n}.$$

where ΔV_j is the observed velocity reduction and $V_A - V_n -$ is the
difference between the velocities of the front and rear parts of
the jet.

The fraction of the jet removed by the target at a given stand-
off is approximately equal to b/P, where b is the plate thickness
and P is the depth to which a jet of the same charge located at the
same distance would penetrate a massive target of the same material
as the plate. Roughly then,

$$\Delta V_j = \frac{b(V_A - V_n)}{P}.$$

37

i.e., the jet velocity reduction caused by influence of the target plate is inversely proportional to the jet penetration depth into a massive target made from the same material and located at the same distance from the charge as the plate. Thus, the distance at which V_j is smallest should equal the optimal charge standoff. As mentioned above, this has been observed for charges with conical aluminum liner. For charges with other liners, the situation is not so clear, possibly because of inaccuracy of the observations.

Kerr Cell Photography of High Speed Phenomena

The metal jets formed from shaped charge liners [1] propagate with velocities exceeding 7000 m/sec. Since the jets are less luminous than the accompanying explosion, their photography by visible light is very difficult. For this reason, many attempts to photograph shaped charge jet travel have been unsuccessful. The first satisfactory photographs were obtained in 1949 (see Figure 9) using flash radiography. Visible light silhouette photographs have been obtained by synchronizing a high intensity light source (electrical discharge yielding a brightness of 3 — 5 · 10^8 candlepower) and a Kerr cell shutter with the phenomenon under study. To obtain the details of the fast moving jet at an object-to-lens distance of 90 — 180 cm, the exposure time must be one microsecond or less. Since it is necessary to use special very high sensitivity, i.e., large-grain, film, the negative must be quite large to preserve the jet propagation details. This is accomplished by using a special lens with focal length 177.8 mm and aperture f/2.5. The aperture is reduced slightly by the Kerr cell and the image is obtained at an effective aperture of f/4.

Figure 19 shows a schematic of the experimental setup. The charge is exploded in a special chamber separated from the observation room by a heavy reinforced concrete wall. Portholes protected by special bulletproof glass are provided in the bombproof chamber walls in order to photograph the phenomena accompanying the explosion. The silhouette of the phenomenon is imaged on a
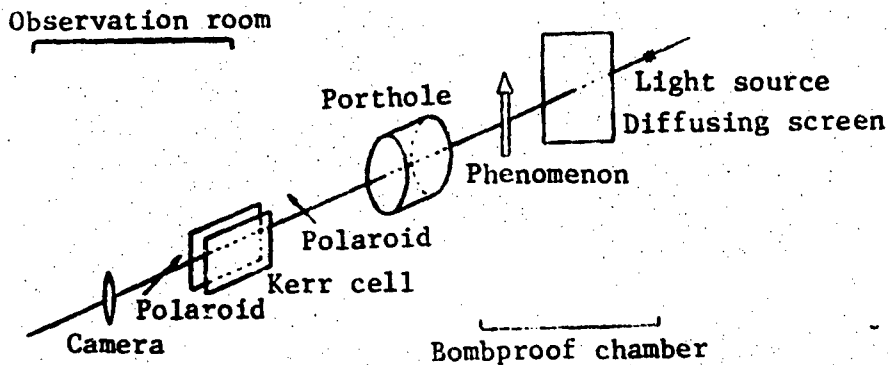
Figure 19. Schematic of experimental setup for Kerr cell photography.

diffusing screen backlighted by the electrical discharge. The Kerr
cell camera with crossed polaroids transmits light only during
the one microsecond interval when a 25 kV pulse is applied to its
electrodes.

Jets Traveling in Air

Attempts to photograph the high speed jets in visible light
led to failure; the jets were not visible on the photos. Such a
picture is shown in Figure 20. Only a small portion of the jet is
visible in the upper part of the picture; the remaining jet is not
seen because of the dark background. Nor were images of the jets
obtained on other photos until the light source was made so brilliant
that the dark region surrounding the jet disappeared and the exposure
was so short that it was possible to stop the motion.

If the dark region at the tip of the jet is magnified several
fold, we can see that it consists of a large number of small
particles traveling at high speed parallel to the jet and vaporizing
continuously because of their rapid motion through the air. To
verify this conclusion, photos were taken of jets passing through
an evacuated glass tube in which the pressure was less than 10^{-3}
mm Hg. In this case, the dark region is not seen at all, the
particles are too small to be visible in the photo, and the metal
vapor is not formed in the absence of air. Figure 20 shows a
picture of a jet formed from a copper cone with flat apex. (In

Figure 20. Jet of hollow charge with copper cone liner with flat apex. We see only a small part of the jet, the rest of the jet is surrounded by a dark region consisting of particles vaporized by rapid motion of the jet through the air.
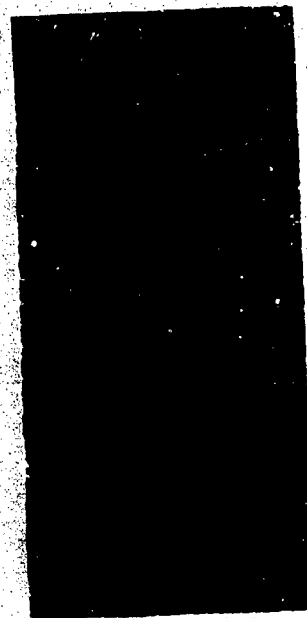
Figure 21. Jet of hollow charge with copper cone liner with truly conical apex. The region surrounding the jet in Figure 20 is nearly eliminated.

mass production it is difficult to produce conical liners with a truly conical pointed apex. However, the lack of a pointed apex is primarily responsible for the appearance of the large cloud seen in Figure 20.) When testing a charge with truly conical brass liner, machined on a lathe, the jet photograph shown in Figure 21 was obtained. In this picture, nearly all the jet is visible, only a small part in the vicinity of the front is obscured by the incandescent metallic cloud formed by the rapid motion of the jet through the air.

Figures 22 and 23 show pictures (prior to and after explosion of jet formation from two hollow lined charges detonated simultaneously.

Figure 22. Two hollow charges with metal liner standing on cardboard sheet and prepared for simultaneous detonation.
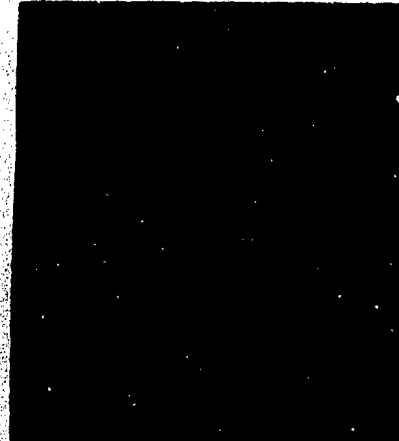
Figure 23. Jets formed from simultaneous detonation of the two charges shown in Figure 22.

Pictures of jet passage through various materials will be presented later. To facilitate interpretation of these pictures, we shall examine two topics: first, the shaped charge detonation phenomenon, and, second, the shock waves and cracking accompanying the detonation, and also other damage to materials as a result of detonation of shaped charges placed on the surfaces of these materials.

Photographs of Detonation Phenomena

The following photographs were obtained of explosions of pentolite (detonation wave propagation velocity 7510 m/sec) and primacord (explosive with detonation wave propagation velocity 6420 m/sec) charges. Figure 24 shows the explosion of a cylindrical pentolite charge (diameter 25.4 mm); the detonation wave proceeding downward. The upper portion of the cloud consists of explosive products of the charge detonator. Measuring the angle between the conical boundary of the region occupied by the explosive products and the charge axis (37.5°) and knowing the detonation wave propagation velocity in pentolite (75 m/sec), we can find the initial velocity of radial expansion of the explosive products,

Figure 25. Detonation of
cylindrical pentolite charge.
Detonation wave propagates
downward with velocity 7510
m/sec.

Figure 26. Simultaneous detona-
ation of two pentolite charges.
Note region of interference of
the two explosive product
regions.

equal to approximately 5800 m/sec. Experimental studies were made
of the interference between the two regions occupied by the
explosive products. Their results are shown in Figures 25 - 27.

Figure 25 shows the explosion of two cylindrical pentolite
charges 25.4 mm in diameter placed on a steel plate so that their
axes are parallel with a distance of 735 mm between centerlines.
The two cylinders were detonated simultaneously. A region of
high luminosity caused by interference between the two regions is
clearly visible. Figure 26 shows the indentations formed in a
101.6 x 101.6 mm mild steel plate after detonation of these charges.
Besides the two circular indentations formed from detonation of
the two charges, we see clearly the cavity arising as a result of
interference between the two explosive product regions. The depth
of the cavity characterizes the order of magnitude of the pressure
within this region; the depth is 3 — 4 mm and approximately equal
to that from the explosion of the charges. Figure 27 shows a
picture of a long pentolite cylinder detonated simultaneously from
both ends. In this case, the region of interference between the

Figure 26. Damage caused in
mild steel plate by pentolite
charges standing on the plate;
detonation was shown in
Figure 25.

Figure 27. Cylindrical pentolite
charge detonated simultaneously
from both ends.

two explosive product region's is
located within the two intersect-
ing cones and a bright luminous
ring is visible.

Photographs of Shock Wave and Cracking in Target Material

High speed Kerr cell photography was used to study shock wave
propagation and fracturing obtained in targets of various materials.
The shock wave formed from explosion in water of a long primacord
charge is shown in Figure 28. We see the slowly propagating dark
central region occupied by the explosive products. Due to the
presence of the air-water interface, the shock wave has definte
curvature. From such photographs, we find that the shock wave
propagation velocity in water ranges from 2200 m/sec near the
primacord charge to 1700 m/sec some distance away from it. At
still greater distance from the charge, the shock wave velocity
probably approaches the velocity of sound in water (1450 m/sec).
A similar picture of a pentolite charge detonated under water (not
shown) indicates that the initial shock wave velocity from the
detonation of such a charge is 3200 m/sec.

It is interesting to study the phenomena occurring in
transparent bodies from high speed jet propagation in them. For
this purpose, 152.4 x 152.4 x 31.8 mm plexiglas blocks were used.

Figure 28. Underwater detona-
tion of primacord charge.
Detonation wave propagates
downward with velocity 6420
m/sec.

Figure 29. Detonation of small
pentolite charge on top of
152.4 x 152.4 x 31.8 mm plexi-
glas slab. Note original shock
wave, reflected wave, and
shattered dark region.

Figure 29 shows a picture of such a plexiglas block after detonation of a cylindrical pentolite charge on its surface. The cylindrical charge was placed to the right of the center on the 152.4 x 31.88 mm surface so that, in addition to the original compression wave, we see the expansion wave reflected from the righthand face. We also see, in the picture, the initial fracturing at the instant of detonation.

Since the detonation wave velocity for most explosives is well known, we can determine the shock wave velocities in transparent bodies by placing the charge on the body surface in a definite fashion and measuring the angle between the surface and the shock wave. Figure 30 shows the shock wave produced by detonation of a pentolite charge lying on the upper face of a plexiglas block. The shock wave velocity varies from 3400 to 2400 m/sec. The lower shock wave velocity limit agrees with the value of the speed of sound.*

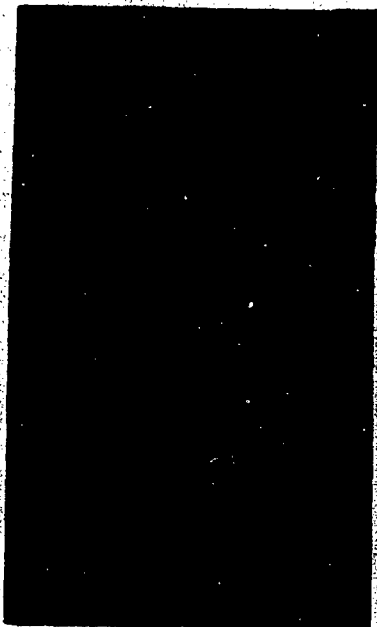*Protzman, T. E. J. Appl. Phys., Vol. 20, 1949, p. 627.

Figure 30. Detonation of cylindrical pentolite charge lying on upper surface of plexi-glas slab.

Figure 31. Metal jet penetrating 12.7 mm thick steel plate. Note intense spalling from the lower surface of the plate.

The next six figures show pictures of metal jet penetration into various materials. In Figure 31, the target is a 12.7 mm thick steel plate.

At the top of the picture we see the region occupied by the explosive products; this region is moving downward, together with the rear part of the jet. Near the steel plate in the vicinity of the point where the jet strikes the target, we see another cloud formed from the fine particles coming from the target material. The pear shaped cloud located under the plate consists of a large number of particles spalled from the steel plate and has quite high density; this cloud obscures the tip of the jet emerging from the steel plate through the hole formed in the plate.

Figure 32 shows a jet penetrating a glass tank filled with water. The jet velocity in the water, in this case, is about 5000 m/sec. Since the shock wave forms an angle of 30° with the jet, its velocity is close to 2500 m/sec, i.e., 1.7 times the speed of sound in water. The jet contour is not visible in the picture, since the liquid near the jet is obviously very turbulent.

Figure 32. Metal jet penetrating water; the jet contour cannot be seen since the liquid near the jet is extremely turbulent.

Figure 33. Metal jet penetrating plexiglas.

Figure 33 shows a jet penetrating a 152.4 x 152.4 x 38.1 mm plexiglas block. The region above the tip of the jet is opaque because the shock wave has reached the lower surface of the plexiglas and the resulting reflected wave has shattered the plexiglas in this region. The picture indicates that the strong compression wave does not shatter the plexiglas.

Figure 34 shows a picture of sequential jet penetration of plexiglas and glass plates 31.8 mm thick, separated by 12.7 mm.

In the plexiglas plate, we see a reflected expansion wave propagating upward from the lower surface and complicating somewhat the cracking pattern. Within the glass, the jet is surrounded by a transparent region which is clearly bounded by a dark line. This dark line cannot be a shock wave, since a shock wave has a conical rather than cylindrical form. It seems probable that, in this region, the glass has melted under the action of the high pressure produced by the tip of the jet. It follows from the energy conservation law that the glass in this region should be heated to
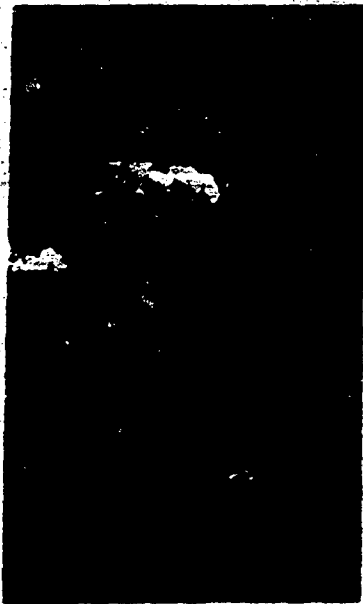
Figure 34.   Metal jet penetrating   Figure 35.   Jet penetrating glass
two identical plexiglas and glass   plate at incidence angle 20°.
plates, separated by 12.7 mm.

temperatures of 1000 — 1500° C. If this assumption is correct,
the dark line around the jet is the boundary between solid and
molten glass.

Figure 35 shows a jet entering glass at an incidence angle of
20°. The boundary between the solid and liquid glass is again
evident. Fracture begins at the lower surface of the glass opposite
the point where the jet enters the target, therefore, the shock
wave has reached the lower surface and been reflected from it.
This photo shows clearly that, when the jet strikes a target of
hard material like glass at a glancing angle, the jet is not
deflected. The experiments also show that the jet is not deflected
when it enters a target of even the hardest steel at an angle.

Figure 36 shows a picture of a metal jet penetrating several
steel targets; here the targets were at approximately a 45° angle
to the jet direction.

47

Figure 30. Photograph of metal jet after perforating two 3.2 mm thick steel targets.

The jet forms a 45° angle with the targets. The slug (on the right) travels relatively slowly and does not participate in target penetration.

While the theory presented above takes into account the increasing length of the jet resulting from the experimentally discovered velocity gradient along the length of the jet, it does not permit satisfactory explanation of the reason for the occurrence of this gradient. The jets formed from the shaped cavity liner are actually much longer than predicted by theory and contain far more material than can be predicted on the basis of the steady-state hydrodynamic theory presented above. While the behavior of the front portions of the jet agrees quite well with the theory, the behavior of the rear portions does not. Flash radiographs of the first stage of jet formation confirmed the predictions of hydrodynamic theory. The pictures of the later stages show a jet emerging from the end of the slug after the collapse process is completed. This gave rise to the postulate that the formation of the front part of the jet follows the steady-state theory while the rear parts of the jet, termed the "afterjet," are formed in an entirely different way, possibly an extrusion or drawing from the slug formed during collapse. The existence of the afterjet can explain why a deep hole is obtained when detonating the charge at a large distance from the target. If jet formation takes place only in accordance with steady-state theory, the penetration depth will be independent of the standoff and for a conical steel liner jet penetrating a steel target, the jet length will be equal to that of the cone generator. In reality, the penetration depth exceeds the generator length by two to four times.

The present version of this theory visualizes the whole jet as formed by one single continuous process. This jet formation process is very similar to that postulated previously for the formation of the front part of the jet. The formation process of the

jet as a whole can be explained by adding one new assumption to the steady-state theory. According to this assumption, the velocities with which the various cone liner elements collapse depend on the original position of the element on the surface of the cone. The collapse velocities decrease continuously from the apex to the base.* The velocities decrease very slowly near the apex but considerably faster near the base. This is expected, since there is less explosive near the base than near the apex and more liner material.

The decreasing liner element collapse velocity as the liner is swept by the detonation wave is the reason for the remarkable effect of greatly increasing jet length and increase of the metal mass entering the jet.

Qualitative ideas resulting from the fact of variability of the collapse velocities can be obtained on the basis of Figure 37, if we recall that the jet velocity and mass of liner metal going into the jet depend on the angle β between the collapsing liner and the cone axis. With increase of β, the jet velocity decreases, but the mass of metal entering the jet increases. We see from Figure 37 that, in the case of decreasing collapse velocities, the angle β is larger than in the constant velocity case.** While the detonation wave travels the distance PQ, the liner element travels from P to J (see Figure 38). The element originally at P' begins to collapse later and with lower velocity; therefore, during this same time, it only reaches M. In the constant collapse velocity case, it would have reached N at this time. Thus, in the case of constant liner collapse velocities, the collapsed surface is also a cone: JNQ is a straight line. In the case of variable collapse velocities, the collapsed surface liner JMQ is not conical, since the element P' collapses with lower velocity than the element P. In our arguments, we naturally assume that the liner is thin and that neighboring

---

*This assumption is obvious; however, the flash radiographs were thought to show that afterjet formation could not be explained so simply. However, a remarkable effect of the velocity gradient on the collapse velocity had been overlooked.

**The increase of the angle β with collapse of the conical liner is shown in Figure 9.
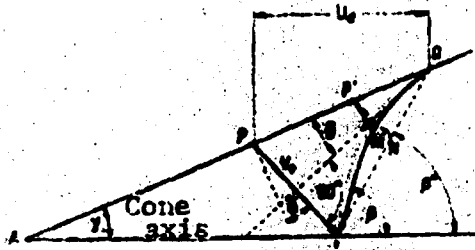
Figure 37.   Cross section
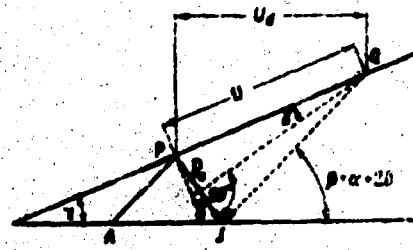showing conical liner collapse.

Figure 38.   Velocity vectors of
element of collapsing conical
liner.

elements have no influence on the collapse velocity of each of the
infinitesimal liner elements.   This assumption is equivalent to the
previous assumption that the liner metal behaves like a perfect
fluid.

A small decrease in the liner element collapse velocity may
produce a relatively large decrease in the jet velocity, since this
velocity decreases because of the decrease of the collapse velocity
and because of increase of the angle β.   Thus, a small V_0 gradient
leads to a larger V_j gradient.

In the case of variable liner element collapse velocities, it
is not possible to select a coordinate system in which the process
will be steady-state, as was done in the case of constant collapse
velocities.   This situation is not a serious handicap, since most
of the relations needed can be obtained — just as in the steady-
state theory — by applying the laws of conservation of mass, energy,
and momentum to the individual conical liner element cut by two
planes perpendicular to the cone axis.   Each element can be con-
sidered independently in a separate coordinate system moving with
the appropriate constant velocity.   There was some thought that
the detonation wave propagation velocity decreases with approach of
the wave to the base of the cone, since less explosive is concen-
trated near the base.   Careful experiments were made to verify these
assumptions.   No changes of the detonation wave velocity U_d were
detected.

50

Since the detonation wave velocity U_d is constant, the impulse given to the liner elements by the wave can be studied in a single inertial coordinate system. Consider a coordinate system moving from P to Q (Figure 37) with the constant velocity $U_1 = U_d \sec \alpha$.

If the impulse imparted by the detonation wave to unit liner mass is constant, a steady-state motion will appear in this coordinate system. We see from Figure 38 that, in this coordinate system, the liner will leave QP downstream of the detonation wave front with the velocity U_1 and travel along PA with this same velocity. Since, in this coordinate system, the resulting detonation wave pressure is everywhere perpendicular to the liner direction of motion, this pressure can change only the direction, but not the magnitude of the liner velocity. In Figure 38, the segment QJ is parallel to PA and equal to QP. If the segments QP and PJ are equal in magnitude to U_1, they represent in the moving coordinate system the liner element velocities, respectively, as the wave front passes through P and during the further motion away from P. The vector $\vec{PJ} = V_0$ is the collapsing liner element velocity in the moving coordinate system traveling with constant velocity, consequently the arguments presented previously can be used here as well. It is evident that the liner element does not move along a line forming the small angle δ with the normal. Referring to Figure 38, we see that

$$\sin \delta = \frac{V_0}{2U_1}.$$ (18)

In the case of decreasing rather than constant impulse imparted by the wave to unit liner mass, the analysis remains the same, if we assume that the liner elements do not interact with each other during collapse. We see from the above discussion that the angle δ will be smaller in this case. The variation of the quantities V_0 and δ depends on the charge shape and the original position of the element in the liner. From Figure 37, we have

$$\beta = \frac{\alpha - \delta}{2}.$$

In the case of liner collapse with constant velocity V_0, the angle β^* is equal to β.

Analysis of the phenomena taking place on the cone axis is now more difficult, since only an accelerated coordinate system can be associated with the liner mass elements concentrated on the axis. From the analyses made in the constant velocity collapse case, we know that each mass element dm splits at the axis into two parts. One part dm_j of the mass goes into the jet, the other part dm_s goes into the slug. For each of the elements, we have the four unknown quantities

$$V_j \text{ and } V_s$$

where V_j and V_s are, respectively, the velocities of dm_j and dm_s in the coordinate system moving with constant velocity. It is obvious from symmetry considerations that the velocities V_j and V_s must be parallel to the axis. To find the four unknown quantities, we have three relations: the equations of conservation of mass, energy, and momentum. One relation is missing. In the case of linear collapse with constant velocity, we use as the additional relation the Bernoulli integral, which cannot be used in the case of variable collapse velocities in the accelerated coordinate system. We take a coordinate system moving with the constant velocity V_1, equal to the instantaneous velocity of the liner elements meeting at the cone axis. On the cone axis, the mass element dm divides into two mass elements dm_j and dm_s, which travel along the axis in opposite directions. Let these elements have the velocities v_j and v_s, respectively, in relation to the moving coordinate system, where the direction of the velocity V_1 is considered positive. Then

$$V_j = V_1 + v_j \text{ and } V_s = V_1 + v_s$$

In the coordinate system adopted, the liner element dm moves toward the axis with relative velocity parallel to the liner element surface. Let the absolute value of this velocity be v. If V_1 and β are the same for all elements, as in the moving uniformly coordinate system, we can use the Bernoulli integral to show that $v_s = -v$. Let
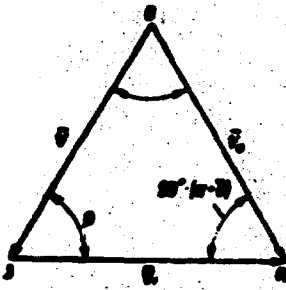
52

Figure 39. Relationship of velocity vectors of liner elements joining at cone axis.

us assume that, in our case also, $v_s = -v$, since this assumption is the most reasonable of all the possible assumptions relative to the dependence of the quantities v_s and v; this simply means that, as the liner element passes through the axis, it alters the direction but not the magnitude of its velocity. From the energy conservation law, we obtain $v_j = v$, thus

$$v_j = -v_s = v. \tag{19}$$

The geometric relation of the velocity vectors for the motion of the liner elements meeting on the axis is shown in Figure 39. The cone axis coincides with JR, and OJ is the liner element moving toward the axis. This element has the velocity $\vec{OR} = V_0$ in the stationary coordinates and the velocity $\vec{OJ} = v$ in the moving coordinates. The velocity of the moving coordinates is $\vec{JR} = V_1$. By the law of sines, we have from Figure 39

$$v = V_0 \frac{\cos(\delta + \beta)}{\cos \delta} \tag{20}$$

and

$$V_1 = V_0 \frac{\cos(\frac{\pi}{2} - \delta - \beta)}{\cos \delta}. \tag{21}$$

The absolute velocities of the jet and slug are, respectively,

$$V_j = V_1 + v_j = V_1 + v$$

and

$$V_s = V_1 + v_s = V_1 - v.$$

Substituting herein (20) and (21) and making some simplifications, we obtain the expressions for the velocities of the jet and slug elements

$$V_j = V_0 \csc \tfrac{\delta}{2} \cos\left(\alpha + \beta - \tfrac{\delta}{2}\right) \tag{22}$$

and

$$V_s = V_0 \sec \tfrac{\delta}{2} \sin\left(\alpha + \beta - \tfrac{\delta}{2}\right). \tag{23}$$

In the special case when the liner collapse velocity V_0 is constant, the angle $\delta = \beta - \alpha + \pi$ is also constant and we have

$$V_j = V_0 \csc \tfrac{\delta}{2} \cos \tfrac{\delta}{2} \tag{2a}$$

and

$$V_s = V_0 \sec \tfrac{\delta}{2} \sin \tfrac{\delta}{2}. \tag{3a}$$

These two relations are identical with (2) and (3), although written in a somewhat simpler form.

We can eliminate δ from (22) and (23) with the aid of (18), which yields

$$V_j = V_0 \csc \tfrac{\delta}{2} \cos\left(\alpha - \tfrac{\beta}{2} + \arcsin \tfrac{V_0}{2V_1}\right). \tag{24}$$

$$V_s = V_0 \sec \tfrac{\delta}{2} \sin\left(\alpha - \tfrac{\beta}{2} + \arcsin \tfrac{V_0}{2V_1}\right). \tag{25}$$

These relations are valid both in the steady-state case when V_0 is the same for all liner elements and in the nonsteady case when V_0 has different values for different liner elements. However, in the steady-state case, the angle β can be expressed in terms of α, U_1, and V_0, and will not appear in the relations for V_j and V_s.

54

Two of the four unknowns, dm_j/dm and dm_s/dm, remain to be calculated. As in the steady-state case, they can be found by using conservation of mass

$$dm = dm_j + dm_s$$

and conservation of momentum

$$-dm\, v \cos\beta = dm_j\, v_j + dm_s\, v_s$$

or, since $v_j = -v_s = v$,

$$dm \cos\beta = dm_s - dm_j.$$

We finally obtain the relations

$$\frac{dm_j}{dm} = \frac{1}{2}(1 - \cos\beta) \tag{26}$$

and

$$\frac{dm_s}{dm} = \frac{1}{2}(1 + \cos\beta). \tag{27}$$

which are identical with the relations (4) obtained in the steady state case.

We see from (26) and (27) how the mass of the conical liner elements divides between the jet and the slug, and from (24) and (25), we find the velocities of the jet and slug elements. The quantities of interest are defined as functions of constant quantities: $U_d = U_x \cos\alpha$ — the detonation wave propagation velocity; and also variable quantities: V_0 — the collapse velocity, and β — the angle between the tangent to the collapsing cone surface and the axis. The collapse velocity V_0 depends on the magnitude of the impulse given by the detonation wave to the liner element. No relation has yet been given for determining β. In the steady state case, it was previously assumed that the collapsing liner remains conical but the angle at the apex of the collapsed liner is greater than for the original cone. In this case, the collapsed liner section contour coincides with the dashed straight line JQ and the angle β^* can be determined from simple trigonometry. In the case of variable velocity V_0, the collapsed liner section contour is a curve

similar to JMQ (see Figure 37) (the curved surface of the collapsed cone can be seen in Figure 9). Thus, β depends on the shape of the collapsing liner near J. Let M (Figure 37) have the cylindrical coordinates (r, z) and P, the original position of M on the liner, have the coordinates (x, x tg α).

Then

$$z = x + V(t-T)\sin A_1 \tag{28}$$

and

$$r = x\,tg\,\alpha - V_0(t-T)\cos A_1 \tag{29}$$

where t is the time elapsed since the detonation wave passed the cone apex, $T = x/U_d = x/U_1 \cos \alpha$ and $A_1 = \alpha + \delta$. The slope of the collapsing liner contour to the axis at any given time can be determined by differentiating r with respect to z for constant t. Since

$$\frac{dA_1}{dx} = \frac{dA_1}{d\delta}\frac{d\delta}{dx} = \frac{1}{U_d}\frac{dA_1}{dt}$$

we have from (12)

$$\frac{\partial r}{\partial x} = \frac{\partial x}{\partial x}\left\{tg\,\alpha - V_0(t-T)\cos A_1 + V\cos\frac{A_1}{U_d} + V A_1(t-T)\sin A_1\right\}. \tag{30}$$

where

$$V_0 = \frac{\partial r}{\partial t} \text{ and } A_1 = \frac{\partial A_1}{\partial t}.$$

Differentiating (28) with respect to z,

$$1 = \frac{\partial x}{\partial x}\left\{1 - V_0(t-T)\sin A_1 - V_0\sin\frac{A_1}{U_d} + V_0 A_1(t-T)\cos A_1\right\}. \tag{31}$$

From (31), with the aid of (30), we obtain the slope of the collapsing liner to the axis at any time

$$\frac{dr}{dz} = \frac{tg\,\alpha - V(t-T)\cos A_1 + V\frac{\cos A_1}{U_d} + V A_1(t-T)\sin A_1}{1 + V_0(t-T)\sin A_1 - V_0\frac{\sin A_1}{U_d} + V_0 A_1(t-T)\cos A_1} \tag{32}$$

56

Substituting $r = 0$ into (12), we obtain the time when the given element reaches the axis

$$t - T = \frac{x \lg \alpha}{V_0 \cos A_0}. \tag{33}$$

After substituting (33) into (32), we obtain

$$\frac{\partial r}{\partial t}\Big|_{r=0} = \lg \beta.$$

Before making this substitution, it is desirable to make some simplifications. From (18), we have

$$2 \sin \delta = \frac{V_0}{V_1} = \frac{V_0 \cos \alpha}{V_d}.$$

Differentiating with respect to x, we obtain

$$2 \cos \delta = \frac{V_0'}{V_1} \quad \text{or} \quad \delta' = \frac{V_0'}{2 V_1 \cos \delta}. \tag{34}$$

Substituting (18), (33), and (34) into (32), we obtain the simple formula

$$\lg \beta = \frac{\cos \alpha + 2 \sin \delta \cos A_0 - x \sin \alpha (1 - \lg A_0 \lg \delta) \frac{V_0'}{V_0}}{\cos \alpha - 2 \cos \delta \cos A_0 + x \sin \alpha (\lg A_0 + \lg \delta) \frac{V_0'}{V_0}}.$$

Since the angle β^* is the value of the angle β which is obtained for $V_0' = 0$, we have, from Figure 37, $2\alpha = \beta^* - \delta$ and $2A_0 = \beta^* + \alpha$, and the last equation can be simplified still further; we obtain

$$\lg \beta = \frac{\sin \beta^* - x \sin \alpha (1 - \lg A_0 \lg \delta) \frac{V_0'}{V_0}}{\cos \beta^* + x \sin \alpha (\lg A_0 + \lg \delta) \frac{V_0'}{V_0}}. \tag{35}$$

The expressions in parentheses in the numerator and denominator of (35) are positive, if the cone angle 2α does not exceed markedly the value normally used in the charges. Therefore, when the collapse velocity decreases from the apex to the base of the cone, i.e., when the derivative V_0' is negative, the angle β is greater than β^*. We

see from (24) and (26) that, with increase of the angle β, the jet velocity decreases and the proportion of the liner mass entering the jet increases.

Now we can explain why the pictures of the late stages of jet formation seem to show the jet issuing from the slug long after completion of the collapse process. This illusion is created by the fact that the last-formed jet and slug elements travel at the same velocity and by the fact that all the jet elements tend to elongate because of the presence of the velocity gradient along the jet length. The last-formed jet and slug elements come from liner elements near the base of the conical cavity. In this region, $V_0 \ll 2U$ and $V_0 \ll xV_0'$ for charges of the type considered. Using these approximations, we obtain from (18), (24), (25), and (35) the following approximate relations: $j \approx j \approx W + a$ and $V_j \approx V \approx V_s$ i.e., the last-formed jet and slug elements travel with approximately the same velocities.

Thus, the formation of the entire jet (including the afterjet) from charges with lined conical cavity is explained by a very simple extension of the previously developed steady state hydrodynamic theory.

Note on Cylindrical Shell Collapse

On the basis of dynamical considerations, we can assume that, when a cylindrical liquid shell contracts radially while retaining its form, very high velocities and pressures should arise and the velocity of the outer shell surface should tend to diminish and that of the inner surface increase.

It seems probable that study of cylindrical liquid shell collapse may be of some assistance in studying the collapse of cylindrical and possibly conical shaped charge metal liners. The collapse of such shells was examined above from the viewpoint of hydrodynamics without account for some details, such as the instantaneous dependence of the pressure on the radial coordinate.

We shall consider cylindrical shells of ideal incompressible fluid whose collapse takes place only in the radial direction (motion along the shell axis is not considered).

We consider a quite long liquid cylindrical shell with external radius r_2 and internal radius r_3 and mass m per unit length. The quantity

$$r_0^2 = r_2^2 - r_3^2$$

remains constant as the shell contracts, since the liquid is assumed incompressible and the motion is only radial. We denote the ratio r_2/r_0 by x. The kinetic energy per unit shell length

$$T = \frac{m}{2}\, \dot{r}_2^2 x^2 \ln \frac{x^2}{x^2-1} .$$

is conserved, if the shell is subjected to the action of only radial contraction and does not change shape. Any shell element can be characterized by a Lagrange hydrodynamic coordinate μ, equal to the mass of the shell material referred to unit length and contained between the outer surface of the shell and an inner coaxial cylinder passing through the given element. The velocity of any shell element characterized by a particular value of μ is

$$\frac{\dot{\mu}}{m}\, r_0 = -\dot{r}_2\, x \sqrt{\frac{x^2}{\left(x^2 \frac{\mu}{m}-1\right)\left(x^2 - \frac{\mu}{m}\right)}}$$

We see from this expression that, as x approaches 1, the inner shell surface velocity approaches infinity and the velocity of the other elements approaches zero. It follows that, during radial contraction of the cylindrical shell without change of its shape, the kinetic energy per unit mass concentrates along the direction toward the shell axis.

It may be shown readily that the pressure is zero at the outer and inner surfaces of the shell and has a maximal value for

$$\frac{\mu}{m} = x^2 - x^2(x^2-1)\ln\frac{x^2}{x^2-1} .$$

The maximum pressure is reached approximately at mid-thickness in the free shell case and approaches the inner surface in the contracting shell case. If the internal and external pressures are zero, the pressure distribution within the shell is given by the formula

$$p = \frac{1}{2} \int \frac{1}{r} \frac{\partial v}{\partial t} dr$$

or

$$p = \frac{r}{m} \frac{1}{\cdots} \left[\ln \frac{r^2}{r^2 - \frac{v}{b}} - \frac{r}{m} \frac{r^2 - 1}{r^2 - \frac{v}{b}} \ln \frac{r^2}{r^2 - 1} \right].$$

We see that very high pressures can be reached.

The shell element velocities and pressures can be calculated, if a constant pressure p acts on the initially free outer surface of the shell and the inner surface is free from the action of any pressure. The radial velocity of a shell element will be

$$\frac{d}{dt} r(x,t) = -\sqrt{\frac{2p}{m}} r_0 \cdot \sqrt{\frac{x(x-1)}{(r^2 - x)^2 \ln \frac{x^2}{x^2 - 1}}}.$$

where x_0 is the intial value of x, and the pressure is given by the formula

$$p_0 = p \left[1 - \frac{\ln \frac{x^2}{x^2 - 1 + \cdots}}{\ln \frac{x^2}{x^2 - 1}} + \frac{\cdots}{x^2(x^2 - 1)} \frac{\ln \frac{x^2}{x^2 - 1}}{\ln^2 \frac{x^2}{x^2 - 1}} - \frac{\cdots}{x^2(x^2 - \frac{v}{b}) \ln \frac{x^2}{x^2 - 1}} \right]$$

The pressure is maximal for

$$\frac{v}{a} = x^2 - \frac{x^2(x^2 - 1)(x^2) - x^2 x \ln \frac{x^2}{x^2 - 1}}{x^4 - x^2 - x^2(x^2 - 1)^2 \ln \frac{x^2}{x^2 - 1}}.$$

To illustrate the preceding general results, we take a specific example. Let $p = 10^{11}$ dynes/cm^2, $r_2 = 2$ cm, $r_0 = 1$ cm, and the liquid shell has the density of steel, i.e., $m = 24.5$ g. Then, for $x = 1.01$, the maximal pressure is reached for $\mu/m = 0.937$ and is equal to $15.6 \cdot 10^{11}$ dynes/cm^2, which is sixteen times greater than the external pressure. The maximal velocity is reached at the inner surface and is equal to about $9.84 \cdot 10^5$ cm/sec.
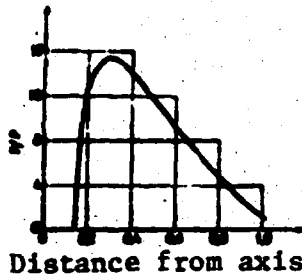
Distance from axis

Figure 40. Pressure distribution in radially contracting cylindrical liquid shell subjected to pressure on outer surface.

In this example, the initial shell inner radius was taken as 1.73 cm, and at the stage of contraction considered, the external and internal surface radii are, respectively, 0.14 and 1.01 cm. The pressure has a maximum at 0.29 cm from the axis (Figure 40).

We can assume that, for a shell of any real compressible liquid, the pressures and velocities will be less than in the case of a shell of ideal incompressible liquid. As a result of the elastic and plastic properties, the behavior of a metallic shell will differ even more from the behavior of the ideal liquid shell. The magnitude of this deviation cannot be predicted at the present time.

Experimental Verification of New Theory of Jet Formation in Shaped Charges with Conical Liners

The experimental study reported herein was undertaken to verify a new theory of jet formation from charges with lined conical cavities. This new theory and the studies described in the beginning of the present paper yield a complete picture of the subject phenomenon.

In the new theory of jet formation, it is assumed that dm, V_0, dm_s, dm_j, V_s, and V_j depend on the position of the subject zonal element on the surface of the cone, i.e., they are functions of x — the distance of the zonal element plane from the apex, measured along the axis. Thus, we examine a conical shell element of mass dm between two planes perpendicular to the axis located at the distances x and $x + dx$ from the apex. The values of m, m_s, and m_j can be found with the aid of the integrals, respectively, of dm, dm_s, and dm_j, taken in the limits from $x = 0$ to x.
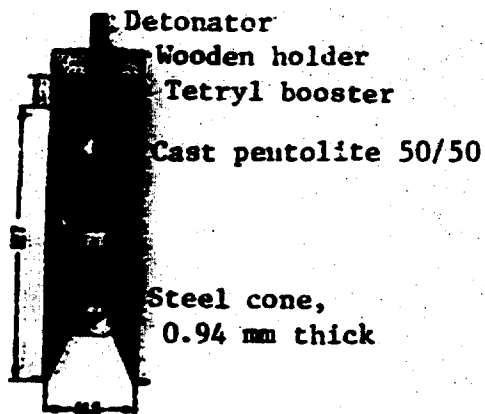
Detonator
Wooden holder
Tetryl booster
Cast pentolite 50/50

Steel cone,
0.94 mm thick

Figure 41. Cross section
of standard charge.

Then all the quantities m, m_i, m_j, V_j and the detonation wave velocity U_d are defined as functions of x; it has also been found that U_d = const. For the three unknown functions $\delta(x)$, $V_0(x)$, and $\beta(x)$, we obtained above the four independent relations (18), (24), (27), and (35). With the aid of two of these four relations, we can express two quantities as functions of the third, substitute the resulting relations into the remaining two, and obtain two independent relations for the third unknown quantity. If the basic assumptions of the theory are sound, the two sets of values obtained for the third unknown from these two relations should be the same.

For experimental verification of the theory, we selected the function β as the third quantity, since it can be determined quite simply from (27) and (35) after substituting therein the values of δ and V_0 from (18) and (24). Since $A = \alpha + \delta$, the quantity β does not appear in the right sides of (27) and (35). We can obtain β directly from experimental data with the aid of (27). The experimental determination of β using (35) is more difficult.

In order to exclude the velocity V_0 from (35), we substitute δ and β from (18) and (27) into (24), then from the resulting expression, we find V_0 and substitute it into (35).

Experiments have been performed with a number of different charge types; however, in the following, we present data relating only to charges of the type shown in Figure 41. The experiments show that the conclusions derived here are also valid for charges of the other types. The charge shown in Figure 41 consists of a cylinder of cast 50/50 pentolite weighing about 227 g and a steel

62

conical liner whose apex angle is 44° (α = 22°) and wall thickness is 0.9 mm. The charge is boosted by a 30 gram pressed tetryl pellet and initiated by an electric blasting cap.

Figure 42. Photographs of: a- grooved conical liner for slug recovery after charge detonation; b- elements of recovered slug;, disintegrated during detonation of charge with liner prepared as shown in a; c- whole recovered slug formed during detonation of charge with ungrooved conical steel liner.

The mass dm of a zonal element is determined by the liner design and can be calculated with reasonable accuracy. However, to avoid errors due to lack of precision in the manufacture of the liner, specimens of the charge were sectioned at accurately determined intervals and each section was weighed individually. This determination of the elementary mass dm yields an accuracy better than 1%.

The values of dm_s as a function of x were determined experimentally very simply. Before lining the charge, the conical liner was cut into individual rings of the same width or grooves were made at regular intervals along the axis. Then the charge was fired in a deep container of water. After firing the charges with either sectioned or grooved liners, the slug, disintegrated into individual elements corresponding to the liner elements, was recovered from the container (see [1]). Figure 42 shows a grooved conical liner, the slug sections recovered after firing a charge with this liner, and the one-piece slug formed when firing a charge with ungrooved conical liner.

While the slug elements can be weighed to within 10^{-4} g, because of statistical fluctuations, the precision of the determination of their weight varied from about 3% for the elements formed from the parts located near the liner apex to 0.3% for the elements formed from the parts located nearer the base. Quite different weight values are obtained for the slug elements formed from the

Conical liner mass, g
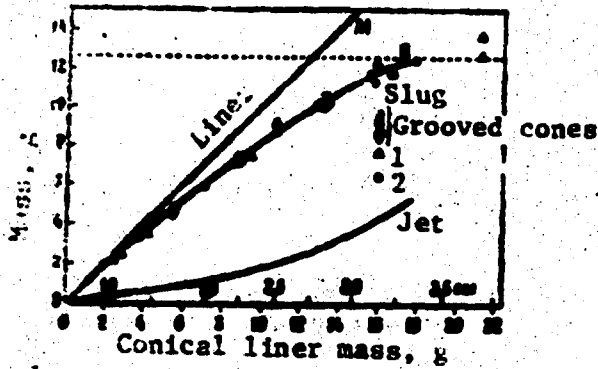
1. Multiple sectioned cones
2. Single sectioned cones

Figure 43. Correlation of slug element masses with liner element masses determined experimentally for sectioned liners and liners with various grooving. Curve of jet mass distribution obtained from experimental curve of slug mass distribution. Total slug mass is 12.6 g.

liner elements located very close to the base, since the slug in this region breaks up irregularly because of the form of the liner. To minimize the influence of this effect on the experimental results, in Figure 43, which shows the slug mass distribution as a function of liner mass, we take as the asymptotic value of the slug mass the average mass of the whole slug formed when firing a charge with ungrooved cone. This figure shows the experimental results obtained by this technique for a series of charges of the type shown in Figure 41. Note that the results of the experiments with grooved liners agree with the results of experiments with presectioned liners.

The curve of jet mass m_j distribution as a function of liner mass shown in Figure 42 was obtained by subtracting the curve for m_s from the straight line M; however, the value of the total jet mass can also be checked experimentally, since the jet is conserved entirely when it travels in water or in ice. The quantities m_j and m_s do not appear in any of the relations (18), (24), (27), and (...) used to check the proposed new theory of jet formation. However, as will be seen later, we must know $m_j(x)$ in order to determine $V_j(x)$, since the velocity V_j is determined from experiment as a function of m_j.

The detonation wave propagation velocity is known to be constant for a given explosive. However, there is evidence that the detonation wave velocity is lower in thin sticks of explosive than in thick sticks. Since the belt of explosive around the conical liner gradually becomes thinner from the apex toward the
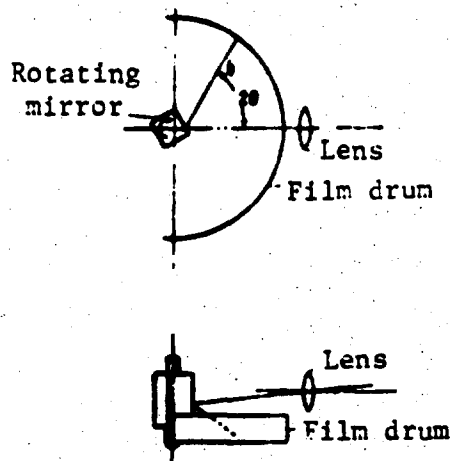
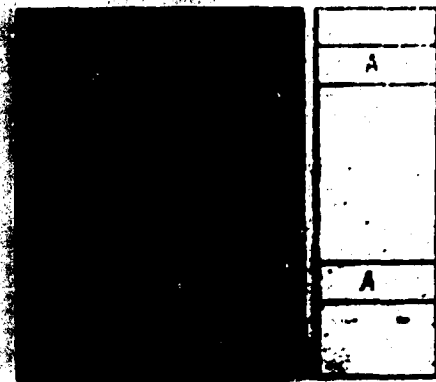Figure 44. Schematic of rotating mirror camera.

Figure 45. Typical detonation wave propagation trace obtained experimentally.

case, it appears that the detonation wave velocity will depend on x. The detonation wave velocity was determined in several ways. The most satisfactory data were obtained by the Jacobs method, in which a photographic record is made of the travel of the luminous detonation wave by means of a rotating mirror camera. A schematic of the camera is shown in Figure 44 and a typical wave trace is shown in Figure 45. The mirror in the camera rotates about an axis parallel to the axis of the test charge. The result is that the detonation wave sweeps along the film and thus permits measuring the time along the axis perpendicular to the direction of travel of the detonation wave image. To produce a sharp trace on the film, the light from the detonating charge is limited by a slit placed near the charge and parallel to its axis. The detonation wave velocity is obtained from the speed of mirror rotation and the slope of the detonation wave trace. The mirror rotational velocity can be varied from 60 rps to 600 rps, and can be measured to within ±0.5 rps. The maximal writing speed on the film is 1.0 mm/μsec. All measurements are made with accuracy to ± 1.0. The measurements showed that the detonation wave velocity for a charge of the type shown in Figure 41 varies only slightly; no significant deviation of the velocity with propagation of the wave near the base of the conical liner from its value for wave propagation near the apex was detected. Thus, we can assume that U_d is independent of x.
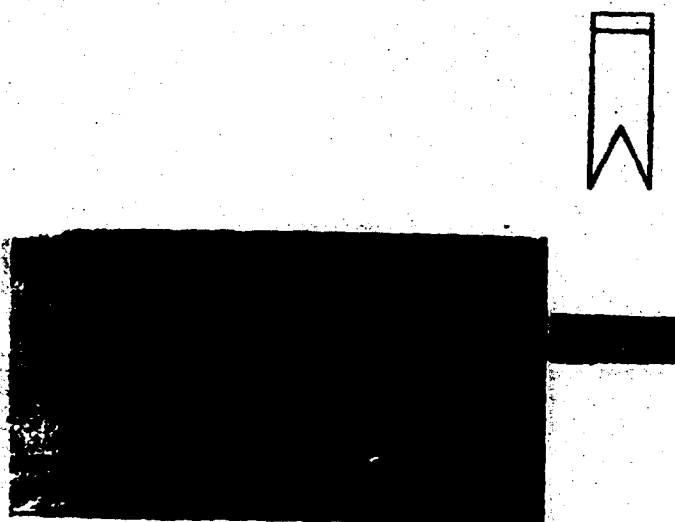
Figure 46a. Schematic of
experiment for determining jet
velocity and typical jet front
trace. Horizontal black streaks
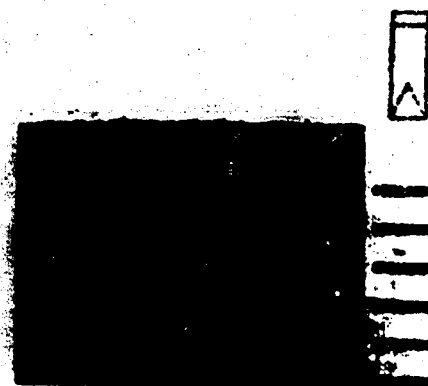are produced by calibration tapes.

Figure 46b. Schematic of
experiment for determining
velocity of various jet
elements and typical jet
trace.

The average detonation wave velocity U_d for the charge type
studied determined from experiment was 7510 m/sec to within $\pm$ 1.0%.

The rotating mirror camera just described can be used to measure
the jet front velocity. The jet travels very fast and when it travels
in air, the jet front is accompanied by a luminous shock wave (see
Figures 21 and 24), which can be recorded on film in the same manner
as the detonation wave is recorded. Since different jet elements
have different velocities, it is necessary to determine the velocity
of each element. To this end, the jet was passed through targets
of different thickness before recording its velocity. When a jet
perforates a target, the elements located at its front are retained
by the target as they strike it, while the elements following behind
pass through the target material practically undisturbed. The
velocity of the remaining part of the jet is then recorded by the
camera. The velocities of different jet elements were recorded
after the jet penetrated targets of different thicknesses. A typical
picture obtained after shooting a jet through a single target is
shown in Figure 46a. If we desire to determine the velocity of each
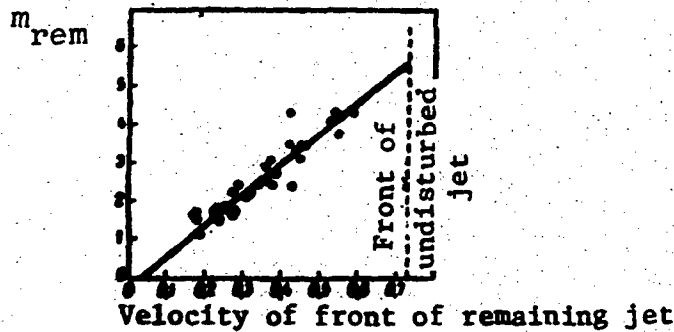jet element, we can shoot a single jet through a series of thin

Figure 47. Experimental correlation of mass of unused (remaining) part of jet m_{rem} and its front velocity.
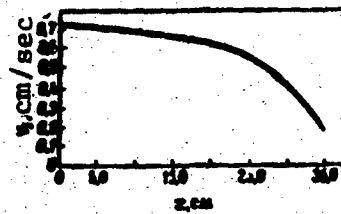
0- inidividual observations; ●- average.

Figure 48. Calculated dependence of jet element velocity V_j on initial position x of corresponding liner element on parent cone.

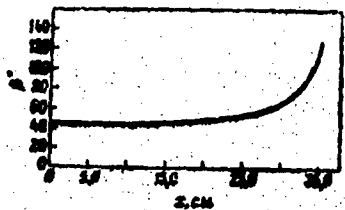targets located at some distance from one another and record the jet front velocity after passing through each of these targets. Velocities recorded in this way are shown in Figure 46b, from which we clearly see that the leading jet elements travel faster than the trailing elements.

However, the target superposition method cannot be used to determine the jet element velocity dependence on the position on the liner of the zonal element from which the given jet element was formed. In order to establish this important dependence, it is necessary to shoot the jet through a single target and then determine, by simple weighing, the mass of the jet elements which have passed through the target. The mass m_j of an individual jet element can be found as the difference between the total jet mass and the mass of its elements which have passed through the target. The velocity of the mass m_j is V_j and is recorded by the camera. Using targets of different thickness, the velocity V_j and the corresponding masses m_j of the various jet elements were determined. The dependence of V_j on m_j was thus found. Using the averaged $m_j(x)$ curve shown in Figure 43, we can determine $V_j(x)$. Figure 47 shows V_j as a function of the jet mass which has passed through the target and Figure 48 shows V_j as a function of x.

Figure 49. Calculated slope of collapsed liner as function of position x of corresponding liner element on parent cone.

In principle, the procedure for determining $V_j(x)$ is simple, but collection of the jet particles after the explosion is exceedingly difficult because of the high penetrating ability of the jet and the tremendous radial stresses arising as the jet propagates in any medium. Initially, water was used as the medium for collecting the jet particles. In later experiments, the jet particles were collected more conveniently and simply in cylinders of ice. In either case, it was necessary to use several gallons of water to collect jet particles weighing about six grams and gaving dimensions from 0.01 to 1 mm. In order to determine the jet mass, the water was carefully filtered and subjected to quantitative chemical analysis. The targets used to remove the leading elements of the jet were naturally made from a material differing from the jet material. The experiment required considerable care to prevent loss of any of the jet particles and avoid contamination of the specimen. The experimental error of the jet collection experiments cannot be evaluated accurately, but probably amounts to about 4%.

We see from (27) that the slope of the m_s versus m curve (see Figure 43) is equal to $\cos^2 \beta/2$. The curve of β versus x obtained on the basis of this relation is plotted in Figure 49. It is difficult to differentiate an experimental curve with a high degree of accuracy. To gain all the accuracy possible from the data, a fifth degree polynomial was used to approximate the curve of Figure 43, using the least squares technique* and the values of β were determined by direct differentiation.

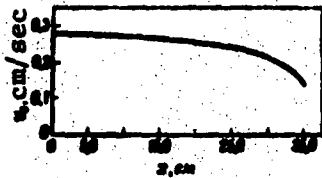*Birge, R. Rev. Mod. Phys., Vol. 19, 1947, pp. 298 - 360.

68

Figure 50. Calculated dependence of liner element collapse velocity V_0 on element position x on parent cone.

The $V_j(x)$ and $\beta(x)$ curves shown in Figures 48 and 49 play a secondary role; they are necessary only for determining $V_0(x)$ with the aid of (24). The final result of this part of the experimental study is shown in Figure 50, which displays a curve of V_0 versus x. These values of $V_0(x)$ can be substituted into (35) to find β and compare the values obtained with the curve of Figure 49. However, it is simpler to substitute the values taken from the curve of Figure 50 into the parametric relations (28) and (29), from which (35) was obtained, and find the values of z and r for different time intervals. From the values of z and r, we can draw the contour of the collapsing liner at any instant of time. The angle between the liner contour and the axis determines the value of the angle β corresponding to the liner element located at the given instant of time on the axis. As an illustration, Figure 51 shows the collapsing liner contour in a particular case. We see from this figure that the liner element 01, located originally near the apex of the conical liner, as a result of collapse, has split into two parts, one of which (0", 1") entered the slug and the other (0''', 1''') — the jet. A liner element located some distance from the apex (cross hatched) as a result of collapse has moved somewhat toward the axis and, together with the neighboring elements, forms the contour of the collapsing part of the liner. In Figure 52, the circles indicate the values of β found graphically and the solid line shows the dependence of β on x, obtained experimentally by determining the slug mass. The agreement of the results is better than could be expected on the basis of experimental accuracy.

It is easy to see why it appears that an afterjet forms. The collapse velocity of the liner elements located near the apex decreases very slowly, just as indicated by the steady state theory; but as the wave approaches the base, the velocities begin to decrease
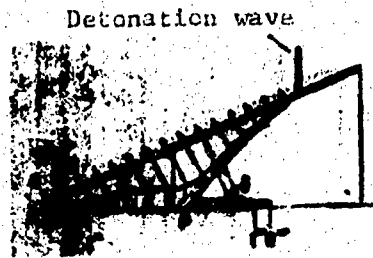
69

Detonation wave

Figure 51. Illustration of graphical solution method.

Positions of liner elements 0, 1, 2, slug elements, and jet elements calculated for an arbitrary instant of time. The values of V_0 and δ were determined from the relations

$$\text{...} \quad \text{and} \quad \text{...}$$

The position of an element which has not yet reached the axis, such as element 9 — 10 (hatched), is determined by the product of V_0 by the time elapsed from the instant the detonation wave passed through the element. To determine the thickness of any element of the collapsing liner, it is sufficient to apply the mass conservation law. For elements such as 0 — 1, which has already reached the axis at the considered time and split into a jet and a slug, the time since their arrival at the axis at 0' and 1', respectively, is determined simply; the velocity of the jet element is known and that of the corresponding slug element can be calculated; thus, the positions 0" and 1" of the slug elements and 0''' and 1''' of the jet elements are determined. To determine the jet and slug diameters, it is necessary to know the distribution of liner mass between the jet and slug. It is obtained from the relation

$$\text{...}$$

The angle between the axis and the tangent to the centerline of the collapsing liner is the angle β.

much more rapidly. As a result of this, it appears that the jet is issuing from the slug long after the completion of the collapse process. However, the experimental data do not indicate any justification for dividing the phenomenon into two parts. In fact, it is strange that, in the jet with nonlinear variations of m, β, and V, with x (see curves in Figures 43, 49, and 50), uniform mass distribution and linear velocity distribution are obtained. The mass of the liner elements and the corresponding angle β increase from the cone apex toward the base. Consequently, we can expect that the front parts of the jet contain far less mass than the rear parts, i.e., the diameter of the front part of the jet is far smaller than that of the rear part; however, the liner collapse
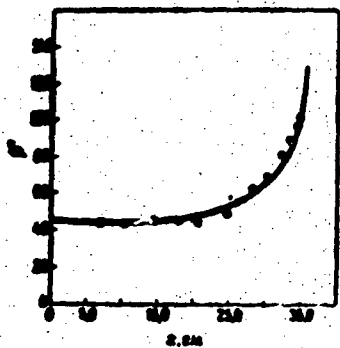
Figure 52. Comparison of results obtained by graphical solution of the parametric equations and experimental determination of slug mass.

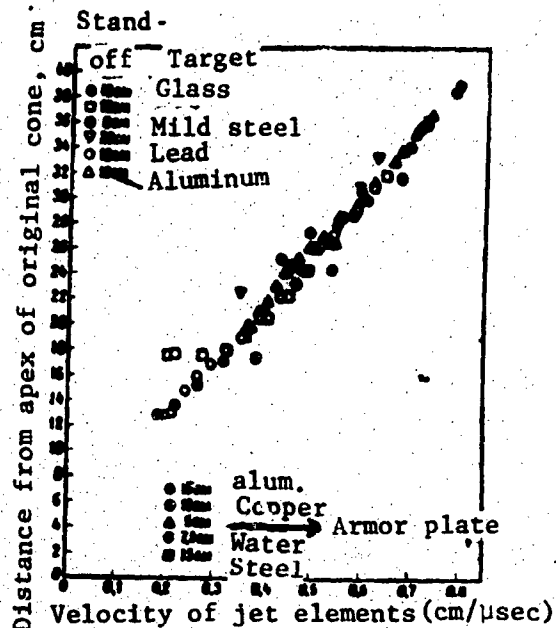—— - experimental curve; 0- graphical solution.

Figure 53. Position of jet elements 50 microseconds after detonation wave passage through cone apex as function of velocity. The data shown were obtained with the aid of a large number of different targets located at various distances.

velocity near the base decreases quite rapidly and it appears that a uniform rate of mass entry into the jet is obtained. The curve of uniform entry of mass into the jet is shown in Figure 47, the liner velocity gradient is shown in Figure 53.

The method, illustrated in Figure 51, can be used to show the process of jet formation and liner conical collapse (see Figure 54).

The results of calculation using this technique can be compared with the pictures obtained by flash radiography (see Figure 9). Although the pictures were obtained for charges of a different type than shown, the agreement of the calculations and observations is very good.

The data shown in Figure 53 were obtained from additional experiments which were not required to verify the theory. These experiments were made with targets of differing thickness and different material, located at various differences from the charges.

Figure 54. Various stages of charge liner collapse.

a- 2.5 microseconds; b- 5 microseconds; c- 10 microseconds; d- 15 microseconds after detonation wave passed the cone apex.

They confirm the assumption that during target penetration, different jet elements do not interact appreciably with each other. The data were obtained using a rotating mirror camera similar to that used in obtaining the photograph shown in Figure 46a.

In our experiments, we did not make use of the fact that the horizontal distance between the point of jet entry into the target (at this point the jet trace in Figure 46a disappears) and the point of jet emergence from the target also determines the time required for target penetration.

If we assume that the velocity of the element located at the front of the jet emerging from the target does not change as it passes through the target material, we can calculate the position of this element at any instant of time. By varying the target thickness, we can select different elements traveling at different velocities to be at the front of the emerging part of the jet. Thus, it is possible to determine the position of any element at any instant of time. Figure 53 shows the locations of the jet elements 50 microseconds after the jet front passed through the base plane of the original liner. The agreement between experimental data obtained with charges located at various distances from the target indicates that the jet element velocities do not change in the penetration process. The agreement between data of experiments with targets of different materials indicates that adjacent elements do not have any marked influence on one another in the penetration process. It is obvious that these assumptions cannot be completely true. The experimental evidence only shows that neither the frictional resistance of the air nor the elastic or plastic stresses within the jet are great enough to noticeably affect the velocities of the jet elements. If the jet travels a distance of 12.2 meters or more, the air resistance increases, primarily because the jet breaks down into particles. As long as the jet is continuous, the air resistance

has very little effect on the velocities of the jet elements. It has not been possible to detect any change in the jet front velocity in the first 0.61 meter of the jet travel, i.e., the jet front recorded by the rotating mirror camera in the jet travel in this distance is not curved.

Thus, the experimental evidence confirms quite well that jet formation from charges with lined conical cavities takes place in a continuous process and that this process is analogous to the hydrodynamic process on the basis of which we previously explained the formation of only the front parts of the jets. The assumption used in the first variant of the theory, that the entire phenomenon is steady state in an appropriately selected coordinate system, permits us to explain the formation of only the first part of the jet and we cannot explain the formation of the afterjet. Previously, the formation of the afterjet had to be explained in some other way. As we would expect, the existence of a velocity gradient along the length of the jet naturally follows from the new theory. It appears that the first variant of the theory can be used to design charges with constant liner collapse velocity, but then there will not be any velocity gradient along the jet, i.e., the jet will not lengthen and, consequently, the penetrating ability of the jet will be less than one fifth the actual value. The experiments show that the charge design shown in Figure 44 is very fortunate in the sense that, when it is fired, a jet is formed with the required velocity gradient which provides both uniform entry of mass into the final jet and linear velocity distribution in the jet.

REFERENCES

1. Bombers B., Zs. f. ges. Schiess- u. Sprengstoffers., 16, 177 (1921).
2. Huttle J., Engng. a. Mining J., 147, 30 5, 68 (1946).
3. Kast M., Spreng- und Zuendstoffe, Braunschweig, 1921.
4. Kast H. und Haid, Zs. f. ges. Schiess- u. Sprengstoffers., 19, 145, 163 (1924).
5. Lewis R. and Clark G., Bull. Univ. Utah, 30 5, 37 (1965).
6. Zodall D., Giornale di chim. ind. ed. appl., 14, 130 (1932).
7. Lupus M., Zs. f. ges. Schiess- u. Sprengstoffers., 29, 63 (1935).
8. Marshall A., J. Soc. Chem. Ind., 39, 35 (1920).
9. Munroe C. E., Scribners Mag., 3, 563 (1888).
10. Munroe C. E., Pop. Sci. Monthly, 55, 444, (1900).
11. Munroe C. E., Am. J. Sci., 36, Ser. 3, 48 (1888).
12. Neumann E., Zs. f. ges. Schiess-Sprengstoffers., 9, 183 (1944).
13. Neumann M., Zs. f. angew. Chem., 34, 2889 (1911).
14. Payman W. and Woodhead D. W., Proc. Roy. Soc., 163, 30 915, 578 (1937).

15. Payman W., Woodhead D. W. and Titman H., *Proc. Roy. Soc.*, 148A, 604 (1935).

16. Stettbacher A., *Brennstoff: Sonderdruck aus chemikalien*, 30, Berlin, 1933—1937.

17. Stettbacher A., *Zs. f. ges. Schiess- u. Sprengstoffw.*, 10, 10 (1915).

18. Stettbacher A., *Schiess- u. Sprengstoffe*, Leipzig, 3 Aufl., 1933.

19. Сухаревский М., *Взрыв и взрывчатые вещества, Москва*.

20. Сухаревский М., *Химия и технология взрывчатых веществ*, 30, 12, (1932); 172, 10 (1932).

21. Torpi V., *Proc. Roy. Soc.*, 148 (15 1935).

22. Forster M., *Versuche mit rauchlosem Schiesspulvern, Berlin*, 1932.

23. Westfaelisch Anhaltsche Sprengstoff A. G., *Verfahren zur Sprengkoerpern und Sprengstoffen*, (1932).

24. Westfaelisch Anhaltsche Sprengstoff A. G., *Zs. f. ges. Schiess- u. Sprengstoffw.*, 6, 388 (1911).

25. Westfaelisch Anhaltsche Sprengstoff A. G. Verfahren zur Herstellung von Sprengkoerpern, Pat. 7 22 1932.

26. Wood R. W., *Proc. Roy. Soc.*, 157, 249 (1936).

27. *Zs. f. ges. Schiess- u. Sprengstoffw.*, 9, 183 (1914).

28. McLemore R. H. *Oil Weekly*, 8 (1946).

29. Worthington A. M., *A Study of Splash*, London, 1918.

30. Milne-Thompson L. L., *Theoretical Hydrodynamics*, London, 1938, ch. 11, 44, chapt. XI

31. Sokolnikoff J. S., *Mathematical Theory of Elasticity*, New York, chapt. 1.

32. Hélie F., *Traité de ballistique expérimentale*, Paris, 1940.

ADDITIONAL REFERENCES

1. Андреев А. Н. и Мейер А. *Горн. журн.*, № 5 (1947)

2. Архипов П., *Горн. журн.*, № 1 (1946).

3. Басов Д., *Механ. трубопровод. и откат. работ*, № 2 (1946).

4. Заболотный Н. *Горн. журн.*, № 8 (1947).

5. Каменка Б. *Механ. трубопровод. и откат. работ*, № 9 (1946)

6. Красельщик В. *Горн. журн.*, № 1 (1949).

7. Королев Ф. А., *ДАН СССР*, 42, 266—267 (1944)

8. Покровский Г. И., *ДАН СССР*, 40 (1945).

9. Покровский Г. И. и Королев Ф. А., *Журн. эксп. и теор. физ.*, 14, 307—312 (1944).

10. Покровский Г. И. и Станюкович К., *Изв. АН СССР, сер. физ.*, 8 (1944).

11. Покровский Г. И. и Ямпольский Б., *Журн. эксп. и теор. физ.*, 16, 263 (1946).

12. Попов С. Г., *Некоторые задачи и методы экспериментальной аэромеханики*, Гостехиздат, 1952 г., § 45.

13. Садовский М., *ДАН СССР*, 40, № 9 (1946).